

arXiv:2303.17007v1 [hep-ex] 29 Mar 2023

Impact of cross-section uncertainties on supernova neutrino spectral parameter fitting in the Deep Underground Neutrino Experiment

- A. Abed Abud,³⁴ B. Abi,¹⁶⁰ R. Acciarri,⁶⁶ M. A. Acero,¹¹ M. R. Adames,¹⁹⁹ G. Adamov,⁷² M. Adamowski,⁶⁶ D. Adams,¹⁹ M. Adinolfi,¹⁸ C. Adriano,²⁹ A. Aduszkiewicz,⁸⁰ J. Aguilar,¹³⁰ Z. Ahmad,²¹¹ J. Ahmed,²¹⁴ B. Aimard,⁵² F. Akbar,¹⁷⁹ K. Allison,⁴² S. Alonso Monsalve,³⁴ M. Alrashed,¹²² A. Alton,¹² R. Alvarez,³⁸ P. Amedo,^{85, 84} J. Anderson,⁷ D. A. Andrade,⁸⁷ C. Andreopoulos,^{182, 132} M. Andreotti,^{94, 67} M. P. Andrews,⁶⁶ F. Andrianala,⁵ S. Andringa,¹³¹ N. Anfimov,¹²⁰ W. L. Anicézio Campanelli,⁶² A. Ankowski,¹⁸⁹ M. Antoniassi,¹⁹⁹ M. Antonova,⁸⁴ A. Antoshkin,¹²⁰ A. Aranda-Fernandez,⁴¹ L. Arellano,¹³⁸ L. O. Arnold,⁴⁴ M. A. Arroyave,⁵⁹ J. Asaadi,²⁰³ A. Ashkenazi,²⁰⁰ L. Asquith,¹⁹⁷ E. Atkin,⁸⁸ D. Auguste,¹⁶⁴ A. Aurisano,³⁹ V. Aushev,¹²⁸ D. Autiero,¹¹¹ M. Ayala-Torres,⁴⁰ F. Azfar,¹⁶⁰ A. Back,⁹¹ H. Back,¹⁶¹ J. J. Back,²¹⁴ I. Bagaturia,⁷² L. Bagby,⁶⁶ N. Balashov,¹²⁰ S. Balasubramanian,⁶⁶ P. Baldi,²³ W. Baldini,⁹⁴ B. Baller,⁶⁶ B. Bambah,⁸¹ R. Banerjee,²²¹ F. Barao,^{131, 113} G. Barenboim,⁸⁴ P. Barham Alzás,³⁴ G. J. Barker,²¹⁴ W. Barkhouse,¹⁵² C. Barnes,¹⁴² G. Barr,¹⁶⁰ J. Barranco Monarca,⁷⁷ A. Barros,¹⁹⁹ N. Barros,^{131, 61} J. L. Barrow,¹³⁹ A. Basharina-Freshville,²⁰⁹ A. Bashyal,⁷ V. Basque,⁶⁶ C. Batchelor,⁵⁸ J.B.R. Battat,²¹⁵ F. Battisti,¹⁶⁰ F. Bay,⁴ M. C. Q. Bazetto,²⁹ J. L. L. Bazo Alba,¹⁷³ J. F. Beacom,¹⁵⁸ E. Bechettoille,¹¹¹ B. Behera,⁶⁸ E. Belchior,¹³⁴ G. Bell,⁵³ L. Bellantoni,⁶⁶ G. Bellettini,^{103, 171} V. Bellini,^{93, 30} O. Beltramello,³⁴ N. Benekos,³⁴ C. Benitez Montiel,^{84, 9} D. Benjamin,¹⁹ F. Bento Neves,¹³¹ J. Berger,⁴³ S. Berkman,⁶⁶ P. Bernardini,^{97, 183} R. M. Berner,¹³ A. Bersani,⁹⁶ S. Bertolucci,^{92, 16} M. Betancourt,⁶⁶ A. Betancur Rodríguez,⁵⁹ A. Bevan,¹⁷⁶ Y. Bezwada,²² A. T. Bezerra,⁶² T. J. Bezerra,¹⁹⁷ J. Bhambure,¹⁹⁴ A. Bhardwaj,¹³⁴ V. Bhatnagar,¹⁶³ M. Bhattacharjee,⁸⁹ M. Bhattacharya,⁶⁶ D. Bhattarai,¹⁴⁸ S. Bhuller,¹⁸ B. Bhuyan,⁸⁹ S. Biagi,¹⁰⁵ J. Bian,²³ K. Biery,⁶⁶ B. Billki,^{14, 109} M. Bishai,¹⁹ A. Bitadze,¹³⁸ A. Blake,¹²⁹ F. D. Blaszczyk,⁶⁶ G. C. Blazey,¹⁵³ D. Blend,¹⁰⁹ E. Blucher,³⁶ J. Boissevain,¹³³ S. Bolognesi,³³ T. Bolton,¹²² L. Bomben,^{98, 108} M. Bonesini,^{98, 144} C. Bonilla-Diaz,³¹ F. Bonini,¹⁹ A. Booth,¹⁷⁶ F. Boran,¹⁴ S. Bordoni,³⁴ A. Borkum,¹⁹⁷ N. Bostan,¹⁰⁹ P. Bour,⁴⁹ J. Bracinik,¹⁵ D. Braga,⁶⁶ D. Brailsford,¹²⁹ A. Branca,⁹⁸ A. Brandt,²⁰³ M. Bravo-Moreno,⁷³ J. Bremer,³⁴ C. Brew,¹⁸² S. J. Brice,⁶⁶ V. Brio,⁹³ C. Brizzolari,^{98, 144} C. Bromberg,¹⁴³ J. Brooke,¹⁸ A. Bross,⁶⁶ G. Brunetti,^{98, 144} M. Brunetti,²¹⁴ N. Buchanan,⁴³ H. Budd,¹⁷⁹ J. Buergi,¹³ G. Caceres V.,²² I. Cagnoli,^{92, 16} T. Cai,²²¹ D. Caiulo,¹¹¹ R. Calabrese,^{94, 67} P. Calafiura,¹³⁰ J. Calcutt,¹⁵⁹ M. Calin,²⁰ L. Calivers,¹³ S. Calvez,⁴³ E. Calvo,³⁸ A. Caminata,⁹⁶ A. Campos Benítez,²¹² D. Caratelli,²⁶ D. Carber,⁴³ J. M. Carceller,²⁰⁹ G. Carini,¹⁹ B. Carlus,¹¹¹ M. F. Carneiro,¹⁹ P. Carniti,⁹⁸ I. Caro Terrazas,⁴³ H. Carranza,²⁰³ N. Carrara,²² L. Carroll,¹²² T. Carroll,²¹⁸ A. Carter,¹⁸⁰ J. F. Castaño Forero,⁶ A. Castillo,¹⁸⁷ C. Castromonte,¹⁰⁶ E. Catano-Mur,²¹⁷ C. Cattadori,⁹⁸ F. Cavalier,¹⁶⁴ G. Cavallaro,⁹⁸ F. Cavanna,⁶⁶ S. Centro,¹⁶² G. Cerati,⁶⁶ A. Cervelli,⁹² A. Cervera Villanueva,⁸⁴ K. Chakraborty,¹⁷⁰ M. Chalifour,³⁴ A. Chappell,²¹⁴ E. Chardonnet,¹⁶⁵ N. Charitonidis,³⁴ A. Chatterjee,¹⁷² S. Chattopadhyay,²¹¹ H. Chen,¹⁹ M. Chen,²³ Y. Chen,^{13, 189} Z. Chen-Wishart,¹⁸⁰ Y. Cheon,²⁰⁸ D. Cherdack,⁸⁰ C. Chi,⁴⁴ S. Childress,⁶⁶ R. Chirco,⁸⁷ A. Chiriacescu,²⁰ N. Chitirasreemadam,^{103, 171} K. Cho,¹²⁵ S. Choate,¹⁵³ D. Chokheli,⁷² P. S. Chong,¹⁶⁸ B. Chowdhury,⁷ A. Christensen,⁴³ D. Christian,⁶⁶ G. Christodoulou,³⁴ A. Chukanov,¹²⁰ M. Chung,²⁰⁸ E. Church,¹⁶¹ V. Cicero,^{92, 16} D. Clapa,²¹³ P. Clarke,⁵⁸ G. Cline,¹³⁰ T. E. Coan,¹⁹³ A. G. Cocco,¹⁰⁰ J. A. B. Coelho,¹⁶⁵ A. Cohen,¹⁶⁵ J. Collot,⁷⁶ E. Conley,⁵⁶ J. M. Conrad,¹³⁹ M. Convery,¹⁸⁹ P. Cooke,¹³² S. Copello,⁹⁶ P. Cova,^{99, 166} C. Cox,¹⁸⁰ L. Cremaldi,¹⁴⁸ L. Cremonesi,¹⁷⁶ J. I. Crespo-Anadón,³⁸ M. Crisler,⁶⁶ E. Cristaldo,^{99, 9} J. Crnkovic,⁶⁶ G. Crone,²⁰⁹ R. Cross,¹²⁹ A. Cudd,⁴² C. Cuesta,³⁸ Y. Cui,²⁵ D. Cussans,¹⁸ J. Dai,⁷⁶ O. Dalager,²³ R. Dallavalle,¹⁶⁵ H. da Motta,³² Z. A. Dar,²¹⁷ R. Darby,¹⁹⁷ L. Da Silva Peres,⁶⁵ C. David,^{221, 66} Q. David,¹¹¹ G. S. Davies,¹⁴⁸ S. Davini,⁹⁶ J. Dawson,¹⁶⁵ K. De,²⁰³ S. De,² R. De Aguiar,²⁹ P. De Almeida,²⁹ P. Debbins,¹⁰⁹ I. De Bonis,⁵² M. P. Decowski,^{150, 3} A. de Gouvêa,¹⁵⁴ P. C. De Holanda,²⁹ I. L. De Icaza Astiz,¹⁹⁷ A. Deisting,¹³⁷ P. De Jong,^{150, 3} A. De la Torre,³⁸ A. Delbart,³³ V. De Leo,^{186, 104} D. Delepine,⁷⁷ M. Delgado,^{98, 144} A. Dell'Acqua,³⁴ N. Delmonte,^{99, 166} P. De Lurgio,⁷ J. R. T. de Mello Neto,⁶⁵ D. M. DeMuth,²¹⁰ S. Dennis,²⁸ C. Densham,¹⁸² P. Denton,¹⁹ G. W. Deptuch,¹⁹ A. De Roeck,³⁴ V. De Romeri,⁸⁴ G. De Souza,²⁹ J. P. Detje,²⁸ R. Devi,¹¹⁷ J. Devine,³⁴ R. Dharmapalan,⁷⁹ M. Dias,²⁰⁷ J. S. Díaz,⁹¹ F. Díaz,¹⁷³ F. Di Capua,^{100, 149} A. Di Domenico,^{186, 104} S. Di Domizio,^{96, 71} S. Di Falco,¹⁰³ L. Di Giulio,³⁴ P. Ding,⁶⁶ L. Di Noto,^{96, 71} E. Diociaiuti,⁹⁵ C. Distefano,¹⁰⁵ R. Diurba,¹³ M. Diwan,¹⁹ Z. Djurcic,⁷ D. Doering,¹⁸⁹ S. Dolan,³⁴ F. Dolek,¹⁴ M. J. Dolinski,⁵⁵ D. Domenici,⁹⁵ L. Domine,¹⁸⁹ S. Donati,^{103, 171} Y. Donon,³⁴ S. Doran,¹¹⁰ D. Douglas,¹⁴³ A. Dragone,¹⁸⁹ F. Drielsma,¹⁸⁹ L. Duarte,²⁰⁷ D. Duchesneau,⁵² K. Duffy,^{160, 66} K. Dugas,²³ P. Dunne,⁸⁸ B. Dutta,²⁰¹ H. Duyang,¹⁹⁰ O. Dvornikov,⁷⁹ D. A. Dwyer,¹³⁰ A. S. Dyshkant,¹⁵³ M. Eads,¹⁵³ A. Earle,¹⁹⁷ S. Edayath,¹¹⁰ D. Edmunds,¹⁴³ J. Eisch,⁶⁶ L. Emberger,^{138, 140} P. Englezos,¹⁸¹ A. Ereditato,²¹⁹ T. Erjavec,²² C. O. Escobar,⁶⁶ J. J. Evans,¹³⁸ E. Ewart,⁹¹

- A. C. Ezeribe,¹⁸⁸ K. Fahey,⁶⁶ L. Fajt,³⁴ A. Falcone,^{98, 144} M. Fani,¹³³ C. Farnese,¹⁰¹ Y. Farzan,¹¹² D. Fedoseev,¹²⁰ J. Felix,⁷⁷ Y. Feng,¹¹⁰ E. Fernandez-Martinez,¹³⁶ F. Ferraro,^{96, 71} G. Ferry,¹⁶⁴ L. Fields,¹⁵⁵ P. Filip,⁴⁸ A. Filkins,¹⁹⁸ F. Filthaut,^{150, 177} R. Fine,¹³³ G. Fiorillo,^{100, 149} M. Fiorini,^{94, 67} V. Fischer,¹¹⁰ R. S. Fitzpatrick,¹⁴² W. Flanagan,⁵¹ B. Fleming,^{36, 219} S. Fogarty,⁴³ W. Foreman,⁸⁷ J. Fowler,⁵⁶ J. Franc,⁴⁹ K. Francis,¹⁵³ D. Franco,²¹⁹ J. Freeman,⁶⁶ J. Fried,¹⁹ A. Friedland,¹⁸⁹ S. Fuess,⁶⁶ I. K. Furic,⁶⁸ K. Furman,¹⁷⁶ A. P. Furmanski,¹⁴⁷ A. Gabrielli,^{92, 16} A. Gago,¹⁷³ H. Gallagher,²⁰⁶ A. Gallas,¹⁶⁴ N. Gallice,^{99, 145} V. Galymov,¹¹¹ E. Gamberini,³⁴ T. Gamble,¹⁸⁸ F. Ganacim,¹⁹⁹ R. Gandhi,⁷⁸ S. Ganguly,⁶⁶ F. Gao,¹⁷² S. Gao,¹⁹ D. Garcia-Gomez,⁷³ M. Á. García-Peris,⁸⁴ S. Gardiner,⁶⁶ D. Gastler,¹⁷ A. Gauch,¹³ J. Gauvreau,¹⁵⁷ P. Gauzzi,^{186, 104} G. Ge,⁴⁴ N. Geffroy,⁵² B. Gelli,²⁹ S. Gent,¹⁹² L. Gerlach,¹⁹ Z. Ghorbani-Moghaddam,⁹⁶ P. Giannaria,²⁹ T. Giannaria,^{94, 67} N. Giangiacomi,²⁰⁵ D. Gibin,^{162, 101} I. Gil-Botella,³⁸ S. Gilligan,¹⁵⁹ A. Gioiosa,¹⁰³ S. Giovannella,⁹⁵ C. Girerd,¹¹¹ A. K. Giri,⁹⁰ C. Giugliano,⁹⁴ D. Gnani,¹³⁰ O. Gogota,¹²⁸ S. Gollapinni,¹³³ K. Gollwitzer,⁶⁶ R. A. Gomes,⁶³ L. V. Gomez Bermeo,¹⁸⁷ L. S. Gomez Fajardo,¹⁸⁷ F. Gonnella,¹⁵ D. Gonzalez-Diaz,⁸⁵ M. Gonzalez-Lopez,¹³⁶ M. C. Goodman,⁷ O. Goodwin,¹³⁸ S. Goswami,¹⁷⁰ C. Gotti,⁹⁸ J. Goudeau,¹³⁴ E. Goudzovski,¹⁵ C. Grace,¹³⁰ R. Gran,¹⁴⁶ E. Granados,⁷⁷ P. Granger,¹⁶⁵ C. Grant,¹⁷ D. Gratieri,⁷⁰ P. Green,¹⁶⁰ S. Greenberg,^{21, 130} L. Greenler,²¹⁸ J. Greer,¹⁸ J. Grenard,³⁴ W. C. Griffith,¹⁹⁷ F. T. Groetschla,³⁴ M. Groh,⁴³ K. Grzelak,²¹³ W. Gu,¹⁹ V. Guarino,⁷ M. Guarise,^{94, 67} R. Guenette,¹³⁸ E. Guerard,¹⁶⁴ M. Guerzoni,⁹² D. Guffanti,⁹⁸ A. Guglielmi,¹⁰¹ B. Guo,¹⁹⁰ Y. Guo,¹⁹⁴ A. Gupta,¹⁸⁹ V. Gupta,^{150, 3} K. K. Guthikonda,¹²⁶ D. Gutierrez,¹⁷⁴ P. Guzowski,¹³⁸ M. M. Guzzo,²⁹ S. Gwon,³⁷ C. Ha,³⁷ K. Haaf,⁶⁶ A. Habig,¹⁴⁶ H. Hadavand,²⁰³ R. Haenni,¹³ L. Hagaman,²¹⁹ A. Hahn,⁶⁶ J. Haiston,¹⁹¹ P. Hamacher-Baumann,¹⁶⁰ T. Hamernik,⁶⁶ P. Hamilton,⁸⁸ J. Han,¹⁷² J. Hancock,¹⁵ F. Happacher,⁹⁵ D. A. Harris,^{221, 66} J. Hartnell,¹⁹⁷ T. Hartnett,¹⁸² J. Harton,⁴³ T. Hasegawa,¹²⁴ C. Hasnip,¹⁶⁰ R. Hatcher,⁶⁶ K. W. Hatfield,²³ A. Hatzikoutelis,¹⁸⁴ C. Hayes,⁹¹ K. Hayrapetyan,¹⁷⁶ J. Hays,¹⁷⁶ E. Hazen,¹⁷ M. He,⁸⁰ A. Heavey,⁶⁶ K. M. Heeger,²¹⁹ J. Heise,¹⁹⁶ S. Henry,¹⁷⁹ M. A. Hernandez Morquecho,⁸⁷ K. Herner,⁶⁶ V. Hewes,³⁹ A. Higuera,¹⁷⁸ C. Hilgenberg,¹⁴⁷ T. Hill,⁸² S. J. Hillier,¹⁵ A. Himmel,⁶⁶ E. Hinkle,³⁶ L.R. Hirsch,¹⁹⁹ J. Ho,⁵⁴ J. Hoff,⁶⁶ A. Holin,¹⁸² T. Holvey,¹⁶⁰ E. Hoppe,¹⁶¹ G. A. Horton-Smith,¹²² M. Hostert,¹⁴⁷ T. Houdy,¹⁶⁴ B. Howard,⁶⁶ R. Howell,¹⁷⁹ J. Hoyos Barrios,¹⁴¹ I. Hristova,¹⁸² M. S. Hronek,⁶⁶ J. Huang,²² R.G. Huang,¹³⁰ Z. Hulcher,¹⁸⁹ G. Iles,⁸⁸ N. Illic,²⁰⁵ A. M. Iliescu,⁹² R. Illingworth,⁶⁶ G. Ingratta,^{92, 16} A. Ioannisian,²²⁰ B. Irwin,¹⁴⁷ L. Isenhower,¹ M. Ismerio Oliveira,⁶⁵ R. Itay,¹⁸⁹ C.M. Jackson,¹⁶¹ V. Jain,² E. James,⁶⁶ W. Jang,²⁰³ B. Jargowsky,²³ F. Jediny,⁴⁹ D. Jena,⁶⁶ Y. S. Jeong,³⁷ C. JesúS-Valls,⁸³ X. Ji,¹⁹ J. Jiang,¹⁹⁴ L. Jiang,²¹² A. Jipa,²⁰ J. H. Jo,¹⁹ F. R. Joaquim,^{131, 113} W. Johnson,¹⁹¹ B. Jones,²⁰³ R. Jones,¹⁸⁸ N. Jovancevic,¹⁵⁶ M. Judah,¹⁷² C. K. Jung,¹⁹⁴ T. Junk,⁶⁶ Y. Jwa,⁴⁴ M. Kabirnezhad,⁸⁸ A. Kaboth,^{180, 182} I. Kadenko,¹²⁸ I. Kakorin,¹²⁰ A. Kalitkina,¹²⁰ D. Kalra,⁴⁴ O. Kamer Koseyan,¹⁰⁹ F. Kamiya,⁶⁴ D. M. Kaplan,⁸⁷ G. Karagiorgi,⁴⁴ G. Karaman,¹⁰⁹ A. Karcher,¹³⁰ Y. Karyotakis,⁵² S. Kasai,¹²⁷ S. P. Kasetti,¹³⁴ L. Kashur,⁴³ I. Katsioulas,¹⁵ A. Kauther,¹⁵³ N. Kazaryan,²²⁰ E. Kearns,¹⁷ P.T. Keener,¹⁶⁸ K.J. Kelly,³⁴ E. Kemp,²⁹ O. Kemularia,⁷² Y. Kermaidic,¹⁶⁴ W. Ketchum,⁶⁶ S. H. Kettell,¹⁹ M. Khabibullin,¹⁰⁷ N. Khan,⁸⁸ A. Khotjantsev,¹⁰⁷ A. Khvedelidze,⁷² D. Kim,²⁰¹ J. Kim,¹⁷⁹ B. King,⁶⁶ B. Kirby,⁴⁴ M. Kirby,⁶⁶ J. Klein,¹⁶⁸ J. Kleykamp,¹⁴⁸ A. Klustova,⁸⁸ T. Kobilarcik,⁶⁶ L. Koch,¹³⁷ K. Koehler,²¹⁸ L. W. Koerner,⁸⁰ D. H. Koh,¹⁸⁹ S. Kohn,^{21, 130} P. P. Koller,¹³ L. Kolupaeva,¹²⁰ D. Korablev,¹²⁰ M. Kordosky,²¹⁷ T. Kosc,⁷⁶ U. Kose,³⁴ V. A. Kostelecký,⁹¹ K. Kothekar,¹⁸ I. Kotler,⁵⁵ V. Kozhukalov,¹²⁰ R. Kralik,¹⁹⁷ L. Kreczko,¹⁸ F. Krennrich,¹¹⁰ I. Kreslo,¹³ W. Kropp,²³ T. Kroupova,¹⁶⁸ S. Kubota,¹³⁸ M. Kubu,³⁴ Y. Kudenko,¹⁰⁷ V. A. Kudryavtsev,¹⁸⁸ S. Kuhlmann,⁷ S. Kulagin,¹⁰⁷ J. Kumar,⁷⁹ P. Kumar,¹⁸⁸ P. Kunze,⁵² R. Kuravi,¹³⁰ N. Kurita,¹⁸⁹ C. Kuruppu,¹⁹⁰ V. Kus,⁴⁹ T. Kutter,¹³⁴ J. Kvashnicka,⁴⁸ D. Kwak,²⁰⁸ T. Labree,¹⁵³ A. Lambert,¹³⁰ B. J. Land,¹⁶⁸ C. E. Lane,⁵⁵ K. Lang,²⁰⁴ T. Langford,²¹⁹ M. Langstaff,¹³⁸ F. Lanni,³⁴ O. Lantwin,⁵² J. Larkin,¹⁹ P. Lasorak,⁸⁸ D. Last,¹⁶⁸ A. Laundrie,²¹⁸ G. Laurenti,⁹² A. Lawrence,¹³⁰ P. Laycock,¹⁹ I. Lazanu,²⁰ M. Lazzaroni,^{99, 145} T. Le,²⁰⁶ S. Leardini,⁸⁵ J. Learned,⁷⁹ P. LeBrun,¹¹¹ T. LeCompte,¹⁸⁹ C. Lee,⁶⁶ V. Legin,¹²⁸ G. Lehmann Miotto,³⁴ R. Lehnert,⁹¹ M. A. Leigui de Oliveira,⁶⁴ M. Leitner,¹³⁰ L. M. Lepin,¹³⁸ S. W. Li,¹⁸⁹ Y. Li,¹⁹ H. Liao,¹²² C. S. Lin,¹³⁰ S. Lin,¹³⁴ D. Lindebaum,¹⁸ R. A. Lineros,³¹ J. Ling,¹⁹⁵ A. Lister,²¹⁸ B. R. Littlejohn,⁸⁷ J. Liu,²³ Y. Liu,³⁶ S. Lockwitz,⁶⁶ T. Loew,¹³⁰ M. Lokajicek,⁴⁸ I. Lomidze,⁷² K. Long,⁸⁸ N. López March,⁸⁴ T. Lord,²¹⁴ J. M. LoSecco,¹⁵⁵ W. C. Louis,¹³³ X.-G. Lu,²¹⁴ K.B. Luk,^{21, 130} B. Lunday,¹⁶⁸ X. Luo,²⁶ E. Luppi,^{94, 67} T. Lux,⁸³ J. Maalmi,¹⁶⁴ D. MacFarlane,¹⁸⁹ A. A. Machado,²⁹ P. Machado,⁶⁶ C. T. Macias,⁹¹ J. R. Macier,⁶⁶ M. MacMahon,²⁰⁹ A. Maddalena,⁷⁵ A. Madera,³⁴ P. Madigan,^{21, 130} S. Magill,⁷ C. Magueur,¹⁶⁴ K. Mahn,¹⁴³ A. Maio,^{131, 61} A. Major,⁵⁶ K. Majumdar,¹³² J. A. Maloney,⁵⁰ M. Man,²⁰⁵ G. Mandrioli,⁹² R. C. Mandujano,²³ J. Maneira,^{131, 61} L. Manenti,²⁰⁹ S. Manly,¹⁷⁹ A. Mann,²⁰⁶ K. Manolopoulos,¹⁸² M. Manrique Plata,⁹¹ S. Manthey Corchado,³⁸ V. N. Manyam,¹⁹ M. Marchan,⁶⁶ A. Marchionni,⁶⁶ W. Marciano,¹⁹ D. Marfatia,⁷⁹ C. Mariani,²¹² J. Maricic,⁷⁹ F. Marinho,¹¹⁴ A. D. Marino,⁴² T. Markiewicz,¹⁸⁹ D. Marsden,¹³⁸ M. Marshak,¹⁴⁷ C. M. Marshall,¹⁷⁹

- J. Marshall,²¹⁴ J. Marteau,¹¹¹ J. Martín-Albo,⁸⁴ N. Martinez,¹²² D.A. Martinez Caicedo,¹⁹¹ F. Martínez López,¹⁷⁶
 P. Martínez Miravé,⁸⁴ S. Martynenko,¹⁹ V. Mascagna,^{98, 108} K. Mason,²⁰⁶ C. Massari,⁹⁸ A. Mastbaum,¹⁸¹
 F. Matichard,¹³⁰ S. Matsuno,⁷⁹ J. Matthews,¹³⁴ C. Mauger,¹⁶⁸ N. Mauri,^{92, 16} K. Mavrokordis,¹³² I. Mawby,²¹⁴
 R. Mazza,⁹⁸ A. Mazzacane,⁶⁶ T. McAskill,²¹⁵ E. McCluskey,⁶⁶ N. McConkey,²⁰⁹ K. S. McFarland,¹⁷⁹ C. McGrew,¹⁹⁴
 A. McNab,¹³⁸ A. Mefodiev,¹⁰⁷ P. Mehta,¹¹⁸ P. Melas,¹⁰ O. Mena,⁸⁴ H. Mendez,¹⁷⁴ P. Mendez,³⁴ D. P. Méndez,¹⁹
 A. Menegolli,^{102, 167} G. Meng,¹⁰¹ M. D. Messier,⁹¹ W. Metcalf,¹³⁴ M. Mewes,⁹¹ H. Meyer,²¹⁶ T. Miao,⁶⁶
 G. Michna,¹⁹² V. Mikola,²⁰⁹ R. Milincic,⁷⁹ G. Miller,¹³⁸ W. Miller,¹⁴⁷ J. Mills,²⁰⁶ O. Mineev,¹⁰⁷ A. Minotti,^{98, 144}
 O. G. Miranda,⁴⁰ S. Miryala,¹⁹ S. Miscetti,⁹⁵ C. S. Mishra,⁶⁶ S. R. Mishra,¹⁹⁰ A. Mislivec,¹⁴⁷ M. Mitchell,¹³⁴
 D. Mladenov,³⁴ I. Mocioiu,¹⁶⁹ K. Moffat,⁵⁷ A. Mogan,⁴³ N. Moggi,^{92, 16} R. Mohanta,⁸¹ T. A. Mohayai,⁶⁶
 N. Mokhov,⁶⁶ J. Molina,⁹ L. Molina Bueno,⁸⁴ E. Montagna,^{92, 16} A. Montanari,⁹² C. Montanari,^{102, 66, 167}
 D. Montanari,⁶⁶ D. Montanino,^{97, 183} L. M. Montaño Zetina,⁴⁰ S. H. Moon,²⁰⁸ M. Mooney,⁴³ A. F. Moor,²⁸
 D. Moreno,⁶ L. Morescalchi,¹⁰³ D. Moretti,⁹⁸ C. Morris,⁸⁰ C. Mossey,⁶⁶ M. Mote,¹³⁴ E. Motuk,²⁰⁹ C. A. Moura,⁶⁴
 J. Mousseau,¹⁴² G. Mouster,¹²⁹ W. Mu,⁶⁶ L. Mualem,²⁷ J. Mueller,⁴³ M. Muether,²¹⁶ F. Muheim,⁵⁸ A. Muir,⁵³
 M. Mulhearn,²² D. Munford,⁸⁰ L. J. Munteanu,³⁴ H. Muramatsu,¹⁴⁷ J. Muraz,⁵² M. Murphy,²¹² T. Murphy,¹⁹⁸
 J. Musser,⁹¹ J. Nachtman,¹⁰⁹ Y. Nagai,⁶⁰ S. Nagu,¹³⁵ M. Nalbandyan,²²⁰ R. Nandakumar,¹⁸² D. Naples,¹⁷²
 S. Narita,¹¹⁵ A. Nath,⁸⁹ A. Navrer-Agasson,¹³⁸ N. Nayak,¹⁹ M. Nebot-Guinot,⁵⁸ K. Negishi,¹¹⁵ A. Nehm,¹³⁷
 J. K. Nelson,²¹⁷ M. Nelson,¹⁰⁹ J. Nesbit,²¹⁸ M. Nessi,^{66, 34} D. Newbold,¹⁸² M. Newcomer,¹⁶⁸ H. Newton,⁵³
 R. Nichol,²⁰⁹ F. Nicolas-Arnaldos,⁷³ A. Nikolica,¹⁶⁸ J. Nikolov,¹⁵⁶ E. Niner,⁶⁶ K. Nishimura,⁷⁹ A. Norman,⁶⁶
 A. Norrick,⁶⁶ P. Novella,⁸⁴ J. A. Nowak,¹²⁹ M. Oberling,⁷ J. P. Ochoa-Ricoux,²³ A. Olivier,¹⁵⁵ A. Olshevskiy,¹²⁰
 T. Olson,⁸⁰ Y. Onel,¹⁰⁹ Y. Onishchuk,¹²⁸ A. Oranday,⁹¹ L. Otiniano Ormachea,^{45, 106} J. Ott,²³ L. Pagani,²²
 G. Palacio,⁵⁹ O. Palamara,⁶⁶ S. Palestini,³⁴ J. M. Paley,⁶⁶ M. Pallavicini,^{96, 71} C. Palomares,³⁸ S. Pan,¹⁷⁰
 W. Panduro Vazquez,¹⁸⁰ E. Pantic,²² V. Paolone,¹⁷² V. Papadimitriou,⁶⁶ R. Papaleo,¹⁰⁵ A. Papanestis,¹⁸²
 S. Paramesvaran,¹⁸ A. Paris,¹⁷⁴ S. Parke,⁶⁶ E. Parozzi,^{98, 144} S. Parsa,¹³ Z. Parsa,¹⁹ S. Parveen,¹¹⁸ M. Parvu,²⁰
 D. Pasciuto,¹⁰³ S. Pascoli,^{57, 16} L. Pasqualini,^{92, 16} J. Pasternak,⁸⁸ J. Pater,¹³⁸ C. Patrick,^{58, 209} L. Patrizii,⁹²
 R. B. Patterson,²⁷ S. J. Patton,¹³⁰ T. Patzak,¹⁶⁵ A. Paudel,⁶⁶ L. Paulucci,⁶⁴ Z. Pavlovic,⁶⁶ G. Pawloski,¹⁴⁷
 D. Payne,¹³² V. Pec,⁴⁸ S. J. M. Peeters,¹⁹⁷ A. Pena Perez,¹⁸⁹ E. Pennacchio,¹¹¹ A. Penzo,¹⁰⁹ O. L. G. Peres,²⁹
 Y. F. Perez Gonzalez,⁵⁷ L. Pérez-Molina,³⁸ C. Pernas,²¹⁷ J. Perry,⁵⁸ D. Pershey,⁵⁶ G. Pessina,⁹⁸ G. Petrillo,¹⁸⁹
 C. Petta,^{93, 30} R. Petti,¹⁹⁰ V. Pia,^{92, 16} L. Pickering,¹⁸⁰ F. Pietropaolo,^{34, 101} V. L. Pimentel,^{46, 29} G. Pinaroli,¹⁹
 K. Plows,¹⁶⁰ R. Plunkett,⁶⁶ C. Pollack,¹⁷⁴ T. Pollman,^{150, 3} F. Pompa,⁸⁴ X. Pons,³⁴ N. Poonthottathil,⁸⁶
 F. Poppi,^{92, 16} S. Pordes,⁶⁶ J. Porter,¹⁹⁷ M. Potekhin,¹⁹ R. Potenza,^{93, 30} B. V. K. S. Potukuchi,¹¹⁷ J. Pozimski,⁸⁸
 M. Pozzato,^{92, 16} S. Prakash,²⁹ T. Prakash,¹³⁰ C. Pratt,²² M. Prest,⁹⁸ F. Psihas,⁶⁶ D. Pugnere,¹¹¹ X. Qian,¹⁹
 J. L. Raaf,⁶⁶ V. Radeka,¹⁹ J. Rademacker,¹⁸ R. Radev,³⁴ B. Radics,²²¹ A. Rafique,⁷ E. Raguzin,¹⁹ M. Rai,²¹⁴
 M. Rajaoalisoa,³⁹ I. Rakhno,⁶⁶ L. Rakotondravohitra,⁵ R. Rameika,⁶⁶ M. A. Ramirez Delgado,¹⁶⁸ B. Ramson,⁶⁶
 A. Rappoldi,^{102, 167} G. Raselli,^{102, 167} P. Ratoff,¹²⁹ R. Ray,⁶⁶ H. Razafinime,³⁹ R. F. Razakamandra,⁵ E. M. Rea,¹⁴⁷
 J. S. Real,⁷⁶ B. Rebel,^{218, 66} R. Rechenmacher,⁶⁶ M. Reggiani-Guzzo,¹³⁸ J. Reichenbacher,¹⁹¹ S. D. Reitzner,⁶⁶
 H. Rejeb Sfar,³⁴ A. Renshaw,⁸⁰ S. Rescia,¹⁹ F. Resnati,³⁴ M. Ribas,¹⁹⁹ S. Riboldi,⁹⁹ C. Riccio,¹⁹⁴ G. Riccobene,¹⁰⁵
 L. C. J. Rice,¹⁷² J. S. Ricol,⁷⁶ A. Rigamonti,³⁴ M. Rigan,¹⁹⁷ E. V. Rincón,⁵⁹ A. Ritchie-Yates,¹⁸⁰ S. Ritter,¹³⁷
 D. Rivera,¹³³ R. Rivera,⁶⁶ A. Robert,⁷⁶ J. L. Rocabado Rocha,⁸⁴ L. Rochester,¹⁸⁹ M. Roda,¹³² P. Rodrigues,¹⁶⁰
 M. J. Rodriguez Alonso,³⁴ J. Rodriguez Rondon,¹⁹¹ S. Rosauro-Alcaraz,¹⁶⁴ P. Rosier,¹⁶⁴ M. Rossella,^{102, 167}
 M. Rossi,³⁴ M. Ross-Lonergan,¹³³ J. Rout,¹¹⁸ P. Roy,²¹⁶ C. Rubbia,⁷⁴ G. Ruiz Ferreira,¹³⁸ B. Russell,¹³⁰
 D. Ruterborries,¹⁷⁹ A. Rybnikov,¹²⁰ A. Saa-Hernandez,⁸⁵ R. Saakyan,²⁰⁹ S. Sacerdoti,¹⁶⁵ S. K. Sahoo,⁹⁰ N. Sahu,⁹⁰
 P. Sala,^{99, 34} A. R. Samana,¹⁸⁵ N. Samios,¹⁹ O. Samoylov,¹²⁰ M. C. Sanchez,⁶⁹ P. Sanchez-Lucas,⁷³ V. Sandberg,¹³³
 D. A. Sanders,¹⁴⁸ D. Sankey,¹⁸² D. Santoro,⁹⁹ N. Saoulidou,¹⁰ P. Sapienza,¹⁰⁵ C. Sarasty,³⁹ I. Sarcevic,⁸ I. Sarra,⁹⁵
 G. Savage,⁶⁶ V. Savinov,¹⁷² G. Scanavini,²¹⁹ A. Scaramelli,¹⁰² A. Scarff,¹⁸⁸ A. Scarpelli,¹⁹ T. Schefke,¹³⁴
 H. Schellman,^{159, 66} S. Schifano,^{94, 67} P. Schlabach,⁶⁶ D. Schmitz,³⁶ A. W. Schneider,¹³⁹ K. Scholberg,⁵⁶
 A. Schukraft,⁶⁶ E. Segreto,²⁹ A. Selyunin,¹²⁰ C. R. Senise,²⁰⁷ J. Senseig,¹⁶⁸ M. H. Shaevitz,⁴⁴ S. Shafaq,¹¹⁸
 F. Shaker,²²¹ P. Shanahan,⁶⁶ H. R. Sharma,¹¹⁷ R. Sharma,¹⁹ R. Kumar,¹⁷⁵ K. Shaw,¹⁹⁷ T. Shaw,⁶⁶ K. Shchablo,¹¹¹
 C. Shepherd-Themistocleous,¹⁸² A. Sheshukov,¹²⁰ W. Shi,¹⁹⁴ S. Shin,¹¹⁹ I. Shoemaker,²¹² D. Shooltz,¹⁴³
 R. Shrock,¹⁹⁴ B. Siddi,⁹⁴ J. Silber,¹³⁰ L. Simard,¹⁶⁴ J. Sinclair,¹⁸⁹ G. Sinev,¹⁹¹ Jaydip Singh,¹³⁵ J. Singh,¹³⁵
 L. Singh,⁴⁷ P. Singh,¹⁷⁶ V. Singh,⁴⁷ S. Singh Chauhan,¹⁶³ R. Sipos,³⁴ C. Sironneau,¹⁶⁵ G. Sirri,⁹² K. Siyeon,³⁷
 K. Skarpaas,¹⁸⁹ E. Smith,⁹¹ P. Smith,⁹¹ J. Smolik,⁴⁹ M. Smy,²³ E.L. Snider,⁶⁶ P. Snopok,⁸⁷ D. Snowden-Ifft,¹⁵⁷
 M. Soares Nunes,¹⁹⁸ H. Sobel,²³ M. Soderberg,¹⁹⁸ S. Sokolov,¹²⁰ C. J. Solano Salinas,¹⁰⁶ S. Söldner-Rembold,¹³⁸
 S.R. Soleti,¹³⁰ N. Solomey,²¹⁶ V. Solovov,¹³¹ W. E. Sondheim,¹³³ M. Sorel,⁸⁴ A. Sotnikov,¹²⁰ J. Soto-Oton,⁸⁴

- A. Sousa,³⁹ K. Soustruznik,³⁵ F. Spagliardi,¹⁶⁰ M. Spanu,^{98, 144} J. Spitz,¹⁴² N. J. C. Spooner,¹⁸⁸ K. Spurgeon,¹⁹⁸ D. Stalder,⁹ M. Stancari,⁶⁶ L. Stanco,^{101, 162} J. Steenis,²² R. Stein,¹⁸ H. M. Steiner,¹³⁰ A. F. Steklain Lisbôa,¹⁹⁹ A. Stepanova,¹²⁰ J. Stewart,¹⁹ B. Stillwell,³⁶ J. Stock,¹⁹¹ F. Stocker,³⁴ T. Stokes,¹³⁴ M. Strait,¹⁴⁷ T. Strauss,⁶⁶ L. Strigari,²⁰¹ A. Stuart,⁴¹ J. G. Suarez,⁵⁹ J. Subash,¹⁵ A. Surdo,⁹⁷ L. Suter,⁶⁶ C. M. Sutera,^{93, 30} K. Sutton,²⁷ Y. Suvorov,^{100, 149} R. Svoboda,²² S. K. Swain,¹⁵¹ B. Szczerbinska,²⁰² A. M. Szelc,⁵⁸ A. Taffara,¹⁰³ N. Talukdar,¹⁹⁰ J. Tamara,⁶ H. A. Tanaka,¹⁸⁹ S. Tang,¹⁹ N. Taniuchi,²⁸ B. Tapia Oregui,²⁰⁴ A. Tapper,⁸⁸ S. Tariq,⁶⁶ E. Tarpara,¹⁹ E. Tatar,⁸² R. Tayloe,⁹¹ A. M. Teklu,¹⁹⁴ P. Tennessen,^{130, 4} M. Tenti,⁹² K. Terao,¹⁸⁹ F. Terranova,^{98, 144} G. Testera,⁹⁶ T. Thakore,³⁹ A. Thea,¹⁸² A. Thompson,²⁰¹ C. Thorn,¹⁹ S. C. Timm,⁶⁶ V. Tishchenko,¹⁹ N. Todorović,¹⁵⁶ L. Tomassetti,^{94, 67} A. Tonazzo,¹⁶⁵ D. Torbunov,¹⁹ M. Torti,^{98, 144} M. Tortola,⁸⁴ F. Tortorici,^{93, 30} N. Tosi,⁹² D. Totani,²⁶ M. Toups,⁶⁶ C. Touramanis,¹³² R. Travaglini,⁹² J. Trevor,²⁷ S. Trilov,¹⁸ W. H. Trzaska,¹²¹ Y. Tsai,²³ Y.-T. Tsai,¹⁸⁹ Z. Tsamalaidze,⁷² K. V. Tsang,¹⁸⁹ N. Tsverava,⁷² S. Z. Tu,¹¹⁶ S. Tufanli,³⁴ C. Tull,¹³⁰ J. Turner,⁵⁷ M. Tuzi,⁸⁴ J. Tyler,¹²² E. Tyley,¹⁸⁸ M. Tzanov,¹³⁴ M. A. Uchida,²⁸ J. Urheim,⁹¹ T. Usher,¹⁸⁹ H. Utaegbulam,¹⁹⁸ S. Uzunyan,¹⁵³ M. R. Vagins,^{123, 23} P. Vahle,²¹⁷ S. Valder,¹⁹⁷ G. D. A. Valdivieso,⁶² E. Valencia,⁷⁷ R. Valentim,²⁰⁷ Z. Vallari,²⁷ E. Vallazza,⁹⁸ J. W. F. Valle,⁸⁴ S. Vallecorsa,³⁴ R. Van Berg,¹⁶⁸ R. G. Van de Water,¹³³ D. Vanegas Forero,¹⁴¹ F. Varanini,¹⁰¹ D. Vargas Oliva,²⁰⁵ G. Varner,⁷⁹ S. Vasina,¹²⁰ N. Vaughan,¹⁵⁹ K. Vaziri,⁶⁶ J. Vega,⁴⁵ S. Ventura,¹⁰¹ A. Verdugo,³⁸ S. Vergani,²⁸ M. A. Vermeulen,¹⁵⁰ M. Verzocchi,⁶⁶ M. Vicenzi,^{96, 71} H. Vieira de Souza,¹⁶⁵ C. Vignoli,⁷⁵ C. Vilela,³⁴ B. Viren,¹⁹ A. Vizcaya-Hernandez,⁴³ T. Vrba,⁴⁹ Q. Vuong,¹⁷⁹ A. V. Waldron,¹⁷⁶ M. Wallbank,³⁹ J. Walsh,¹⁴³ T. Walton,⁶⁶ H. Wang,²⁴ J. Wang,¹⁹¹ L. Wang,¹³⁰ M.H.L.S. Wang,⁶⁶ X. Wang,⁶⁶ Y. Wang,²⁴ K. Warburton,¹¹⁰ D. Warner,⁴³ M.O. Wascko,⁸⁸ D. Waters,²⁰⁹ A. Watson,¹⁵ K. Wawrowska,^{182, 197} P. Weatherly,⁵⁵ A. Weber,^{137, 66} M. Weber,¹³ H. Wei,¹³⁴ A. Weinstein,¹¹⁰ D. Wenman,²¹⁸ M. Wetstein,¹¹⁰ J. Whilhelmi,²¹⁹ A. White,²⁰³ A. White,²¹⁹ L. H. Whitehead,²⁸ D. Whittington,¹⁹⁸ M. J. Wilking,¹⁹⁴ A. Wilkinson,²⁰⁹ C. Wilkinson,¹³⁰ Z. Williams,²⁰³ F. Wilson,¹⁸² R. J. Wilson,⁴³ W. Wisniewski,¹⁸⁹ J. Wolcott,²⁰⁶ J. Wolfs,¹⁷⁹ T. Wongjirad,²⁰⁶ A. Wood,⁸⁰ K. Wood,¹³⁰ E. Worcester,¹⁹ M. Worcester,¹⁹ M. Wospakrik,⁶⁶ K. Wresilo,²⁸ C. Wret,¹⁷⁹ S. Wu,¹⁴⁷ W. Wu,⁶⁶ W. Wu,²³ M. Wurm,¹³⁷ J. Wyenberg,⁵⁴ Y. Xiao,²³ I. Xiotidis,⁸⁸ B. Yaegg,³⁹ N. Yahlahi,⁸⁴ E. Yandel,²⁶ G. Yang,¹⁹⁴ K. Yang,¹⁶⁰ T. Yang,⁶⁶ A. Yankelevich,²³ N. Yershov,¹⁰⁷ K. Yonehara,⁶⁶ Y. S. Yoon,³⁷ T. Young,¹⁵² B. Yu,¹⁹ H. Yu,¹⁹ H. Yu,¹⁹⁵ J. Yu,²⁰³ Y. Yu,⁸⁷ W. Yuan,⁵⁸ R. Zaki,²²¹ J. Zalesak,⁴⁸ L. Zambelli,⁵² B. Zamorano,⁷³ A. Zani,⁹⁹ L. Zazueta,²¹⁷ G. P. Zeller,⁶⁶ J. Zenanno,⁶⁶ K. Zeug,²¹⁸ C. Zhang,¹⁹ S. Zhang,⁹¹ Y. Zhang,¹⁷² M. Zhao,¹⁹ E. Zhivun,¹⁹ E. D. Zimmerman,⁴² S. Zucchelli,^{92, 16} J. Zuklin,⁴⁸ V. Zutshi,¹⁵³ and R. Zwaska⁶⁶

(The DUNE Collaboration)

¹Abilene Christian University, Abilene, TX 79601, USA

²University of Albany, SUNY, Albany, NY 12222, USA

³University of Amsterdam, NL-1098 XG Amsterdam, The Netherlands

⁴Antalya Bilim University, 07190 Döşemealtı/Antalya, Turkey

⁵University of Antananarivo, Antananarivo 101, Madagascar

⁶Universidad Antonio Nariño, Bogotá, Colombia

⁷Argonne National Laboratory, Argonne, IL 60439, USA

⁸University of Arizona, Tucson, AZ 85721, USA

⁹Universidad Nacional de Asunción, San Lorenzo, Paraguay

¹⁰University of Athens, Zografou GR 157 84, Greece

¹¹Universidad del Atlántico, Barranquilla, Atlántico, Colombia

¹²Augustana University, Sioux Falls, SD 57197, USA

¹³University of Bern, CH-3012 Bern, Switzerland

¹⁴Beykent University, Istanbul, Turkey

¹⁵University of Birmingham, Birmingham B15 2TT, United Kingdom

¹⁶Università del Bologna, 40127 Bologna, Italy

¹⁷Boston University, Boston, MA 02215, USA

¹⁸University of Bristol, Bristol BS8 1TL, United Kingdom

¹⁹Brookhaven National Laboratory, Upton, NY 11973, USA

²⁰University of Bucharest, Bucharest, Romania

²¹University of California Berkeley, Berkeley, CA 94720, USA

²²University of California Davis, Davis, CA 95616, USA

²³University of California Irvine, Irvine, CA 92697, USA

²⁴University of California Los Angeles, Los Angeles, CA 90095, USA

²⁵University of California Riverside, Riverside CA 92521, USA

²⁶University of California Santa Barbara, Santa Barbara, California 93106 USA

²⁷California Institute of Technology, Pasadena, CA 91125, USA

²⁸University of Cambridge, Cambridge CB3 0HE, United Kingdom

- ²⁹Universidade Estadual de Campinas, Campinas - SP, 13083-970, Brazil
³⁰Università di Catania, 2 - 95131 Catania, Italy
³¹Universidad Católica del Norte, Antofagasta, Chile
³²Centro Brasileiro de Pesquisas Físicas, Rio de Janeiro, RJ 22290-180, Brazil
³³IRFU, CEA, Université Paris-Saclay, F-91191 Gif-sur-Yvette, France
³⁴CERN, The European Organization for Nuclear Research, 1211 Meyrin, Switzerland
³⁵Institute of Particle and Nuclear Physics of the Faculty of Mathematics and Physics of the Charles University, 180 00 Prague 8, Czech Republic
³⁶University of Chicago, Chicago, IL 60637, USA
³⁷Chung-Ang University, Seoul 06974, South Korea
³⁸CIEMAT, Centro de Investigaciones Energéticas, Medioambientales y Tecnológicas, E-28040 Madrid, Spain
³⁹University of Cincinnati, Cincinnati, OH 45221, USA
⁴⁰Centro de Investigación y de Estudios Avanzados del Instituto Politécnico Nacional (Cinvestav), Mexico City, Mexico
⁴¹Universidad de Colima, Colima, Mexico
⁴²University of Colorado Boulder, Boulder, CO 80309, USA
⁴³Colorado State University, Fort Collins, CO 80523, USA
⁴⁴Columbia University, New York, NY 10027, USA
⁴⁵Comisión Nacional de Investigación y Desarrollo Aeroespacial, Lima, Peru
⁴⁶Centro de Tecnología da Informação Renato Archer, Campinas, SP - CEP 13069-901
⁴⁷Central University of South Bihar, Gaya, 824236, India
⁴⁸Institute of Physics, Czech Academy of Sciences, 182 00 Prague 8, Czech Republic
⁴⁹Czech Technical University, 115 19 Prague 1, Czech Republic
⁵⁰Dakota State University, Madison, SD 57042, USA
⁵¹University of Dallas, Irving, TX 75062-4736, USA
⁵²Laboratoire d'Annecy de Physique des Particules, Univ. Grenoble Alpes, Univ. Savoie Mont Blanc, CNRS, LAPP-IN2P3, 74000 Annecy, France
⁵³Daresbury Laboratory, Cheshire WA4 4AD, United Kingdom
⁵⁴Dordt University, 700 7th St NE, Sioux Center, IA 51250, USA
⁵⁵Drexel University, Philadelphia, PA 19104, USA
⁵⁶Duke University, Durham, NC 27708, USA
⁵⁷Durham University, Durham DH1 3LE, United Kingdom
⁵⁸University of Edinburgh, Edinburgh EH8 9YL, United Kingdom
⁵⁹Universidad EIA, Envigado, Antioquia, Colombia
⁶⁰Eötvös Loránd University, 1053 Budapest, Hungary
⁶¹Faculdade de Ciências da Universidade de Lisboa - FCUL, 1749-016 Lisboa, Portugal
⁶²Universidade Federal de Alfenas, Poços de Caldas - MG, 37715-400, Brazil
⁶³Universidade Federal de Goias, Goiania, GO 74690-900, Brazil
⁶⁴Universidade Federal do ABC, Santo André - SP, 09210-580, Brazil
⁶⁵Universidade Federal do Rio de Janeiro, Rio de Janeiro - RJ, 21941-901, Brazil
⁶⁶Fermi National Accelerator Laboratory, Batavia, IL 60510, USA
⁶⁷University of Ferrara, Ferrara, Italy
⁶⁸University of Florida, Gainesville, FL 32611-8440, USA
⁶⁹Florida State University, Tallahassee, FL, USA
⁷⁰Fluminense Federal University, 9 Icaraí Niterói - RJ, 24220-900, Brazil
⁷¹Università degli Studi di Genova, Genova, Italy
⁷²Georgian Technical University, Tbilisi, Georgia
⁷³University of Granada & CAFPE, 18002 Granada, Spain
⁷⁴Gran Sasso Science Institute, L'Aquila, Italy
⁷⁵Laboratori Nazionali del Gran Sasso, L'Aquila AQ, Italy
⁷⁶University Grenoble Alpes, CNRS, Grenoble INP, LPSC-IN2P3, 38000 Grenoble, France
⁷⁷Universidad de Guanajuato, Guanajuato, C.P. 37000, Mexico
⁷⁸Harish-Chandra Research Institute, Jhunsi, Allahabad 211 019, India
⁷⁹University of Hawaii, Honolulu, HI 96822, USA
⁸⁰University of Houston, Houston, TX 77204, USA
⁸¹University of Hyderabad, Gachibowli, Hyderabad - 500 046, India
⁸²Idaho State University, Pocatello, ID 83209, USA
⁸³Institut de Física d'Altes Energies (IFAE)—Barcelona Institute of Science and Technology (BIST), Barcelona, Spain
⁸⁴Instituto de Física Corpuscular, CSIC and Universitat de València, 46980 Paterna, Valencia, Spain
⁸⁵Instituto Galego de Física de Altas Enerxías, University of Santiago de Compostela, Santiago de Compostela, 15782, Spain
⁸⁶Indian Institute of Technology Kanpur, Uttar Pradesh 208016, India
⁸⁷Illinois Institute of Technology, Chicago, IL 60616, USA
⁸⁸Imperial College of Science Technology and Medicine, London SW7 2BZ, United Kingdom
⁸⁹Indian Institute of Technology Guwahati, Guwahati, 781 039, India
⁹⁰Indian Institute of Technology Hyderabad, Hyderabad, 502285, India

- ⁹¹Indiana University, Bloomington, IN 47405, USA
⁹²Istituto Nazionale di Fisica Nucleare Sezione di Bologna, 40127 Bologna BO, Italy
⁹³Istituto Nazionale di Fisica Nucleare Sezione di Catania, I-95123 Catania, Italy
⁹⁴Istituto Nazionale di Fisica Nucleare Sezione di Ferrara, I-44122 Ferrara, Italy
⁹⁵Istituto Nazionale di Fisica Nucleare Laboratori Nazionali di Frascati, Frascati, Roma, Italy
⁹⁶Istituto Nazionale di Fisica Nucleare Sezione di Genova, 16146 Genova GE, Italy
⁹⁷Istituto Nazionale di Fisica Nucleare Sezione di Lecce, 73100 - Lecce, Italy
⁹⁸Istituto Nazionale di Fisica Nucleare Sezione di Milano Bicocca, 3 - I-20126 Milano, Italy
⁹⁹Istituto Nazionale di Fisica Nucleare Sezione di Milano, 20133 Milano, Italy
¹⁰⁰Istituto Nazionale di Fisica Nucleare Sezione di Napoli, I-80126 Napoli, Italy
¹⁰¹Istituto Nazionale di Fisica Nucleare Sezione di Padova, 35131 Padova, Italy
¹⁰²Istituto Nazionale di Fisica Nucleare Sezione di Pavia, I-27100 Pavia, Italy
¹⁰³Istituto Nazionale di Fisica Nucleare Laboratori Nazionali di Pisa, Pisa PI, Italy
¹⁰⁴Istituto Nazionale di Fisica Nucleare Sezione di Roma, 00185 Roma RM, Italy
¹⁰⁵Istituto Nazionale di Fisica Nucleare Laboratori Nazionali del Sud, 95123 Catania, Italy
¹⁰⁶Universidad Nacional de Ingeniería, Lima 25, Perú
¹⁰⁷Institute for Nuclear Research of the Russian Academy of Sciences, Moscow 117312, Russia
¹⁰⁸University of Insubria, Via Ravasi, 2, 21100 Varese VA, Italy
¹⁰⁹University of Iowa, Iowa City, IA 52242, USA
¹¹⁰Iowa State University, Ames, Iowa 50011, USA
¹¹¹Institut de Physique des 2 Infinis de Lyon, 69622 Villeurbanne, France
¹¹²Institute for Research in Fundamental Sciences, Tehran, Iran
¹¹³Instituto Superior Técnico - IST, Universidade de Lisboa, Portugal
¹¹⁴Instituto Tecnológico de Aeronáutica, São José dos Campos, Brazil
¹¹⁵Iwate University, Morioka, Iwate 020-8551, Japan
¹¹⁶Jackson State University, Jackson, MS 39217, USA
¹¹⁷University of Jammu, Jammu-180006, India
¹¹⁸Jawaharlal Nehru University, New Delhi 110067, India
¹¹⁹Jeonbuk National University, Jeonrabuk-do 54896, South Korea
¹²⁰Joint Institute for Nuclear Research, Dzhelepov Laboratory of Nuclear Problems 6 Joliot-Curie, Dubna, Moscow Region, 141980 RU
¹²¹University of Jyväskylä, FI-40014, Finland
¹²²Kansas State University, Manhattan, KS 66506, USA
¹²³Kavli Institute for the Physics and Mathematics of the Universe, Kashiwa, Chiba 277-8583, Japan
¹²⁴High Energy Accelerator Research Organization (KEK), Ibaraki, 305-0801, Japan
¹²⁵Korea Institute of Science and Technology Information, Daejeon, 34141, South Korea
¹²⁶K L University, Vaddeswaram, Andhra Pradesh 522502, India
¹²⁷National Institute of Technology, Kure College, Hiroshima, 737-8506, Japan
¹²⁸Taras Shevchenko National University of Kyiv, 01601 Kyiv, Ukraine
¹²⁹Lancaster University, Lancaster LA1 4YB, United Kingdom
¹³⁰Lawrence Berkeley National Laboratory, Berkeley, CA 94720, USA
¹³¹Laboratório de Instrumentação e Física Experimental de Partículas, 1649-003 Lisboa and 3004-516 Coimbra, Portugal
¹³²University of Liverpool, L69 7ZE, Liverpool, United Kingdom
¹³³Los Alamos National Laboratory, Los Alamos, NM 87545, USA
¹³⁴Louisiana State University, Baton Rouge, LA 70803, USA
¹³⁵University of Lucknow, Uttar Pradesh 226007, India
¹³⁶Madrid Autónoma University and IFT UAM/CSIC, 28049 Madrid, Spain
¹³⁷Johannes Gutenberg-Universität Mainz, 55122 Mainz, Germany
¹³⁸University of Manchester, Manchester M13 9PL, United Kingdom
¹³⁹Massachusetts Institute of Technology, Cambridge, MA 02139, USA
¹⁴⁰Max-Planck-Institut, Munich, 80805, Germany
¹⁴¹University of Medellín, Medellín, 050026 Colombia
¹⁴²University of Michigan, Ann Arbor, MI 48109, USA
¹⁴³Michigan State University, East Lansing, MI 48824, USA
¹⁴⁴Università del Milano-Bicocca, 20126 Milano, Italy
¹⁴⁵Università degli Studi di Milano, I-20133 Milano, Italy
¹⁴⁶University of Minnesota Duluth, Duluth, MN 55812, USA
¹⁴⁷University of Minnesota Twin Cities, Minneapolis, MN 55455, USA
¹⁴⁸University of Mississippi, University, MS 38677 USA
¹⁴⁹Università degli Studi di Napoli Federico II, 80138 Napoli NA, Italy
¹⁵⁰Nikhef National Institute of Subatomic Physics, 1098 XG Amsterdam, Netherlands
¹⁵¹National Institute of Science Education and Research (NISER), Odisha 752050, India
¹⁵²University of North Dakota, Grand Forks, ND 58202-8357, USA
¹⁵³Northern Illinois University, DeKalb, IL 60115, USA

- ¹⁵⁴Northwestern University, Evanston, Il 60208, USA
¹⁵⁵University of Notre Dame, Notre Dame, IN 46556, USA
¹⁵⁶University of Novi Sad, 21102 Novi Sad, Serbia
¹⁵⁷Occidental College, Los Angeles, CA 90041
¹⁵⁸Ohio State University, Columbus, OH 43210, USA
¹⁵⁹Oregon State University, Corvallis, OR 97331, USA
¹⁶⁰University of Oxford, Oxford, OX1 3RH, United Kingdom
¹⁶¹Pacific Northwest National Laboratory, Richland, WA 99352, USA
¹⁶²Università degli Studi di Padova, I-35131 Padova, Italy
¹⁶³Panjab University, Chandigarh, 160014 U.T., India
¹⁶⁴Université Paris-Saclay, CNRS/IN2P3, IJCLab, 91405 Orsay, France
¹⁶⁵Université Paris Cité, CNRS, Astroparticule et Cosmologie, Paris, France
¹⁶⁶University of Parma, 43121 Parma PR, Italy
¹⁶⁷Università degli Studi di Pavia, 27100 Pavia PV, Italy
¹⁶⁸University of Pennsylvania, Philadelphia, PA 19104, USA
¹⁶⁹Pennsylvania State University, University Park, PA 16802, USA
¹⁷⁰Physical Research Laboratory, Ahmedabad 380 009, India
¹⁷¹Università di Pisa, I-56127 Pisa, Italy
¹⁷²University of Pittsburgh, Pittsburgh, PA 15260, USA
¹⁷³Pontificia Universidad Católica del Perú, Lima, Perú
¹⁷⁴University of Puerto Rico, Mayaguez 00681, Puerto Rico, USA
¹⁷⁵Punjab Agricultural University, Ludhiana 141004, India
¹⁷⁶Queen Mary University of London, London E1 4NS, United Kingdom
¹⁷⁷Radboud University, NL-6525 AJ Nijmegen, Netherlands
¹⁷⁸Rice University, Houston, TX 77005
¹⁷⁹University of Rochester, Rochester, NY 14627, USA
¹⁸⁰Royal Holloway College London, TW20 0EX, United Kingdom
¹⁸¹Rutgers University, Piscataway, NJ, 08854, USA
¹⁸²STFC Rutherford Appleton Laboratory, Didcot OX11 0QX, United Kingdom
¹⁸³Università del Salento, 73100 Lecce, Italy
¹⁸⁴San Jose State University, San José, CA 95192-0106, USA
¹⁸⁵Universidade Estadual de Santa Cruz, CEP 45662-000, Ilheús, Bahia-BA, Brazil
¹⁸⁶Sapienza University of Rome, 00185 Roma RM, Italy
¹⁸⁷Universidad Sergio Arboleda, 11022 Bogotá, Colombia
¹⁸⁸University of Sheffield, Sheffield S3 7RH, United Kingdom
¹⁸⁹SLAC National Accelerator Laboratory, Menlo Park, CA 94025, USA
¹⁹⁰University of South Carolina, Columbia, SC 29208, USA
¹⁹¹South Dakota School of Mines and Technology, Rapid City, SD 57701, USA
¹⁹²South Dakota State University, Brookings, SD 57007, USA
¹⁹³Southern Methodist University, Dallas, TX 75275, USA
¹⁹⁴Stony Brook University, SUNY, Stony Brook, NY 11794, USA
¹⁹⁵Sun Yat-Sen University, Guangzhou, 510275
¹⁹⁶Sanford Underground Research Facility, Lead, SD, 57754, USA
¹⁹⁷University of Sussex, Brighton, BN1 9RH, United Kingdom
¹⁹⁸Syracuse University, Syracuse, NY 13244, USA
¹⁹⁹Universidade Tecnológica Federal do Paraná, Curitiba, Brazil
²⁰⁰Tel Aviv University, Tel Aviv-Yafo, Israel
²⁰¹Texas A&M University, College Station, Texas 77840
²⁰²Texas A&M University - Corpus Christi, Corpus Christi, TX 78412, USA
²⁰³University of Texas at Arlington, Arlington, TX 76019, USA
²⁰⁴University of Texas at Austin, Austin, TX 78712, USA
²⁰⁵University of Toronto, Toronto, Ontario M5S 1A1, Canada
²⁰⁶Tufts University, Medford, MA 02155, USA
²⁰⁷Universidade Federal de São Paulo, 09913-030, São Paulo, Brazil
²⁰⁸Ulsan National Institute of Science and Technology, Ulsan 689-798, South Korea
²⁰⁹University College London, London, WC1E 6BT, United Kingdom
²¹⁰Valley City State University, Valley City, ND 58072, USA
²¹¹Variable Energy Cyclotron Centre, 700 064 West Bengal, India
²¹²Virginia Tech, Blacksburg, VA 24060, USA
²¹³University of Warsaw, 02-093 Warsaw, Poland
²¹⁴University of Warwick, Coventry CV4 7AL, United Kingdom
²¹⁵Wellesley College, Wellesley, MA 02481, USA
²¹⁶Wichita State University, Wichita, KS 67260, USA
²¹⁷William and Mary, Williamsburg, VA 23187, USA

²¹⁸*University of Wisconsin Madison, Madison, WI 53706, USA*

²¹⁹*Yale University, New Haven, CT 06520, USA*

²²⁰*Yerevan Institute for Theoretical Physics and Modeling, Yerevan 0036, Armenia*

²²¹*York University, Toronto M3J 1P3, Canada*

(Dated: March 31, 2023)

A primary goal of the upcoming Deep Underground Neutrino Experiment (DUNE) is to measure the \mathcal{O} MeV neutrinos produced by a Galactic core-collapse supernova if one should occur during the lifetime of the experiment. The liquid-argon-based detectors planned for DUNE are expected to be uniquely sensitive to the ν_e component of the supernova flux, enabling a wide variety of physics and astrophysics measurements. A key requirement for a correct interpretation of these measurements is a good understanding of the energy-dependent total cross section $\sigma_{\nu e}$ for charged-current

absorption on argon. In the context of a simulated extraction of supernova spectral parameters from a toy analysis, we investigate the impact of $\sigma_{\nu e}$ modeling uncertainties on DUNE's supernova neutrino physics sensitivity for the first time. We find that the currently large theoretical uncertainties on $\sigma_{\nu e}$ must be substantially reduced before the ν_e flux parameters can be extracted reliably: in the absence of external constraints, a measurement of the integrated neutrino luminosity with less than 10% bias with DUNE requires $\sigma_{\nu e}$ to be known to about 5%. The neutrino spectral shape parameters can be known to better than 10% for a 20% uncertainty on the cross-section scale, although they will be sensitive to uncertainties on the shape of $\sigma_{\nu e}$. A direct measurement of low-energy ν_e -argon scattering would be invaluable for improving the theoretical precision to the needed level.

I. INTRODUCTION

A massive star ($M \gtrsim 8 M_\odot$) employs nuclear fusion to sustain itself by first consuming lighter elements such as hydrogen and helium and later consuming heavier elements. In the canonical narrative, at the end of the star's lifetime, the innermost nickel-iron core can no longer undergo nuclear fusion. Gravity causes the core to collapse into a proto-neutron star. Neutron degeneracy stalls the collapse; the core rebounds and produces shock waves which propagate outward from the core. Once the shock waves breach the surface of the star, they expel stellar material and leave behind a compact remnant. This process is referred to as a core-collapse supernova.

A core collapse releases 99% of the star's gravitational potential energy via neutrinos in a prompt burst lasting several seconds [1]. While the proto-neutron star traps photons and other particles with electromagnetic and strong interactions, neutrinos easily escape because they interact weakly. The neutrino flux is expected to contain interesting signatures related to different phenomena occurring during a core-collapse supernova [2–6], including insight into the explosion mechanism. While the neutrinos detected from SN1987A [7–10] did help to confirm the basic outline of the core-collapse supernova process, they did not provide tight constraints on astrophysical models. Additional neutrino signals from core-collapse supernovae observed in detectors worldwide [11] will provide data to study the mechanism behind the core collapse, as well as information on the properties of neutrinos themselves.

Obtaining a high-statistics measurement of core-collapse supernova neutrinos is among the primary physics goals for the Deep Underground Neutrino Experiment (DUNE). To detect these low-energy neutrinos, DUNE will utilize its far detector (relative to the beam at Fermilab) located 1.5 km underground at the Sanford

Underground Research Facility in South Dakota. The DUNE far detector is currently planned to consist of four liquid argon time projection chambers (LArTPCs) each with a total volume of around seventeen kilotons [12]. These LArTPC detectors will be sensitive to interactions of neutrinos in the few tens of MeV range [13].

Among large neutrino experiments, DUNE will be uniquely sensitive to the ν_e component of the supernova signal via the charged-current reaction



The ν_e component of the supernova neutrino flux is expected to contain unique features which make its future detection with DUNE a valuable scientific opportunity [12].

The neutrinos generated by a core-collapse supernova have much lower energies (few to tens of MeV) than the GeV-scale neutrino beams of interest for DUNE's accelerator-based oscillation physics program. Below 100 MeV, no measurements of charged-current neutrino-argon cross sections are currently available [14], and competing theoretical calculations have significant discrepancies [15]. While the importance of obtaining a precise understanding of neutrino-nucleus scattering at accelerator energies is widely recognized [16–18], and the impact of related uncertainties has been studied in detail by the DUNE collaboration [19], the same cannot yet be said for the tens of MeV regime relevant for supernova neutrino detection. This situation exists despite shared analysis challenges between the two energy scales: in both cases, a reliable cross-section model is needed for neutrino calorimetry, efficiency estimation, and removal of some classes of background events. Theoretical uncertainties on the cross-section model provide an important limitation on the achievable experimental precision.

In this paper, we examine for the first time the impact of cross-section uncertainties on the interpretation of a

possible future observation of supernova neutrinos with DUNE. No attempt is made here to be comprehensive in either the uncertainty budget or in the analysis topics considered; for instance, these studies assume that the distance to the core collapse is known precisely. Our aim is instead to explore how variations of the adopted model of the neutrino-argon cross section affect the results of a measurement of simulated data. The present study is restricted to variations of $\sigma(E_\nu)$, the total charged-current cross section as a function of neutrino energy. The studies presented in this paper use simplified assumptions about detector response, but a realistic efficiency for DUNE includes sensitivity to neutrino energies as low as 5 MeV [20]. Although these studies require an assumption about DUNE’s expected energy resolution, similar studies performed in Ref. [12] show that the results are not sensitive to the specific choice of energy resolution [21]. Variations to other aspects of the neutrino interaction model, including predictions of exclusive final-state differential distributions and the description of ${}^{40}\text{K}^*$ nuclear de-excitations, as well as subdominant neutral-current and $\bar{\nu}_e$ charged-current interactions, are left to future work, both for simplicity and because the related uncertainties are difficult to fully quantify at present.

The algorithm used in our measurements to extract supernova ν_e flux parameters from simulated DUNE data is presented in Sec. II. In Sec. III, we describe three different procedures for varying the $\nu_e - {}^{40}\text{Ar}$ total cross section, and the impact on the simulated measurements is examined for each approach. We discuss the results, their implications for DUNE’s future supernova neutrino effort, and prospects for the future in Sec. IV and conclude in Sec. V.

II. SUPERNOVA PARAMETER FITTING

A. Pinched-thermal form

A commonly-used representation for the supernova neutrino fluence (i.e., the time integral of the flux) Φ passing through the Earth is the pinched-thermal form [22, 23]:

$$\Phi(E_\nu) = \frac{\varepsilon}{4\pi d^2} \mathcal{N} \left(\frac{E_\nu}{\langle E_\nu \rangle} \right)^\alpha \exp \left[-(\alpha + 1) \frac{E_\nu}{\langle E_\nu \rangle} \right], \quad (2)$$

where

$$\mathcal{N} \equiv \frac{(\alpha + 1)^{\alpha+1}}{\langle E_\nu \rangle^2 \Gamma(\alpha + 1)}, \quad (3)$$

is a normalization constant, ε is the neutrino luminosity, E_ν is the neutrino energy, $\langle E_\nu \rangle$ is the mean neutrino energy (related to the temperature of the supernova), and d is the distance from the supernova to Earth. The “pinching parameter” α describes the shape of the tails of the neutrino energy distribution.

The expression in Eq. 2 may be used to represent either an instantaneous flux (with dimensions of neutrinos per area per time) or a fluence in a specific time interval (flux integrated over time, with dimensions of neutrinos per area), depending on the units used for ε . In the instantaneous case, the parameters $\langle E_\nu \rangle$ (MeV) and α (dimensionless) are implicitly time-dependent, while for the time-integrated case they should be interpreted as average values. The time-integrated spectrum is also well described by Eq. 2, and the parameters should be interpreted as being applied to the fluence spectrum over the entire burst. For simplicity, we choose to consider only the time-integrated neutrino flux in which ε may be expressed in ergs. A distance of $d = 10$ kiloparsecs (kpc) is assumed throughout. Different values of the flux parameters describe each neutrino species separately (i.e., the ν_e parameters are not the same as the $\bar{\nu}_e$ or $\nu_x \equiv \nu_\mu, \nu_\tau, \bar{\nu}_\mu, \bar{\nu}_\tau$ parameters), but only the ν_e portion of the flux is of interest for the present study given its dominance in the expected supernova signal in DUNE [12]. For the studies in this paper, we assume equipartition between flavors, i.e., $\alpha_{\nu_e} = \alpha_{\bar{\nu}_e} = \alpha_{\nu_x}$ and $\varepsilon_{\nu_e} = \varepsilon_{\bar{\nu}_e} = \varepsilon_{\nu_x}$, and we adopt the hierarchy in Ref. [24] for the mean neutrino energies. The simulated measurements considered here involve an extraction of the ν_e pinched-thermal flux parameters ε , $\langle E_\nu \rangle$, and α from the reconstructed neutrino energy spectrum expected for DUNE. Figure 1 shows fluences calculated for a pinched-thermal flux.

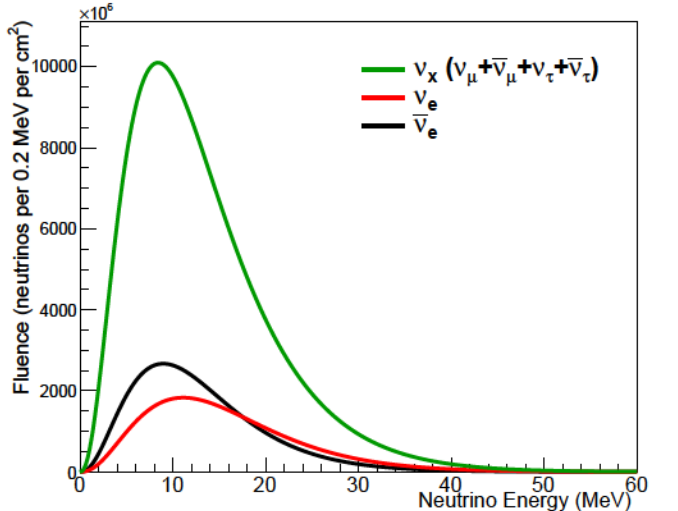


FIG. 1. Pinched-thermal neutrino fluences for a supernova at a distance of 10 kpc. Following Ref. [25], the results are time-integrated over the first ten seconds. The initial fluence parameter values for ν_e are $(\alpha^0, \langle E_\nu \rangle^0, \varepsilon^0) = (2.5, 9.5 \text{ MeV}, 5 \times 10^{52} \text{ ergs})$, for $\bar{\nu}_e$ are $(\alpha^0, \langle E_\nu \rangle^0, \varepsilon^0) = (2.5, 12.0 \text{ MeV}, 5 \times 10^{52} \text{ ergs})$, and for ν_x are $(\alpha^0, \langle E_\nu \rangle^0, \varepsilon^0) = (2.5, 15.6 \text{ MeV}, 5 \times 10^{52} \text{ ergs})$. Normal mass ordering and Mikheyev-Smirnov-Wolfenstein (MSW) resonances [26, 27] were assumed via Equation 5.

B. SNOwGLoBES

Beyond the neutrino-argon cross section, the supernova signal observed by DUNE will also be affected by the supernova flux, the detector response, efficiency, and energy reconstruction. The SuperNova Observatories with General Long-Baseline Experiment Simulator (SNOwGLoBES) software incorporates the effect of detector response factors, including the cross section, into a simulated supernova neutrino signal. This widely used, open-source event rate calculation tool offers a quick option to model the DUNE far detector response for supernova neutrino signals [28].

SNOwGLoBES requires several inputs to perform the simulation, including a cross-section model and a “smearing matrix,” i.e., a transfer matrix that can be used to calculate a reconstructed neutrino energy spectrum when applied to the true neutrino energy spectrum (see Fig. 2). In addition, there is an assumed post-smearing detection efficiency. SNOwGLoBES makes use of GLoBES [29] software to convolve a specified flux with a cross section and a smearing matrix. We used fluxes given by Eq. 2 and computed the smearing matrix using simulated

Ar interactions produced by the MARLEY event generator [30, 31] with 10% Gaussian smearing applied to the visible energy. The exact value of 10% is modestly optimistic for DUNE’s expected capabilities, but the results are not sensitive to the specific value [12].

For our simulated signal predictions, we adopted one of the more optimistic neutrino energy reconstruction scenarios described in Ref. [30]. Under this scenario, the reconstructed neutrino energy is taken to be the *visible energy* $\epsilon_{\text{vis}}^{\text{reco}}$ defined by the expression

$$\epsilon_{\text{vis}}^{\text{reco}} = \min(\epsilon_{\text{bind}} + \epsilon_e + \mathcal{T} + \mathcal{T}_{\text{ch}}) \quad (4)$$

Here, $\epsilon_{\text{bind}}^{\text{min}} = 0.99$ MeV is the minimum possible change in nuclear binding energy for the charged-current reaction, ϵ_e is the total energy of the outgoing electron, \mathcal{T} is the summed energy of all de-excitation γ -rays, and \mathcal{T}_{ch} is the summed kinetic energy of all final-state charged hadrons.

SNOwGLoBES outputs binned energy spectra (Asimov data sets) corresponding to different detector parameter assumptions and for given pinched-thermal spectral parameters (α, β, γ). Figure 3 shows the two types of SNOwGLoBES output energy spectra; “interaction rates” refers to the energies of neutrinos that interacted (before detector response), while “observed rates” refers to the prediction of the observed spectra in the proposed detector. The observed rates are what the proposed DUNE far detector would observe during the first ten seconds of a 10 kpc supernova burst.

C. Mass ordering assumptions in SNOwGLoBES

The different neutrino flavor amplitudes will change as they move through the collapsing star and in the vac-

uum of space toward Earth. These flavor transitions will affect the flux that reaches the DUNE detector, and consequently the flavor transitions will affect the $\nu_e - \bar{\nu}_e$ event rates. SNOwGLoBES provides a simple evaluation of the matter effect for both normal and inverted mass ordering assumptions; we assumed $\Delta m^2 = 33.71$ and the following relations for flavor content for normal mass ordering (NMO) according to the standard prescription in Ref. [32]:

$$\nu_e = \cos(\theta) \nu_1 + \sin(\theta) \nu_2 \quad (5a)$$

$$\bar{\nu}_e = \cos(\theta) \bar{\nu}_1 + \sin(\theta) \bar{\nu}_2 \quad (5b)$$

Here, ν_i is the flux for one (or more) neutrino flavor, and $\bar{\nu}_i$ is the flux before the flavor transition. In the presence of flavor transitions, all produced flavors matter for the observed ν_e rate at Earth. To take into account effects produced by flavor transitions, we define a range of flux parameters for ν_i and $\bar{\nu}_i$ using the θ parameters and the relations outlined in Section II A.

D. Forward fitting

The resulting reconstructed energy spectra from SNOwGLoBES are influenced by the choice of pinched-thermal flux parameters. Measurements of the spectral parameters might contain biases partly introduced by uncertainties in our input assumptions such as the cross-section model. We developed an algorithm that fits a reconstructed neutrino energy spectrum to obtain estimated values of the pinched-thermal parameters; this then enables us to study the impact of the $\nu_e - \bar{\nu}_e$ cross section model on the fit results.

Our algorithm employs a “forward-fitting” approach as an alternative to unfolding; in a forward-fitting approach, a theory prediction convolved with the response of a given detector is compared directly with data. Forward fitting requires two inputs: (1) a reconstructed neutrino energy spectrum produced by SNOwGLoBES for a supernova at a given distance and (2) a “true” set of pinched-thermal parameters (θ_{true}). The algorithm uses this spectrum as a “true spectrum” to compare against a reference grid of reconstructed energy spectra generated with many different combinations of (θ_{grid}). In this paper, the true spectrum refers to the assumed true spectrum under test in the algorithm. To quantify goodness-of-fit, the algorithm uses a χ^2 function defined by

$$\chi^2 = \frac{1}{N} \sum_{i=1}^N \left(\frac{N_i^{\text{obs}} - N_i^{\text{true}}}{\sigma_i} \right)^2 \quad (6)$$

Here N_i is the number of reconstructed energy bins, N_i^{obs} is the number of events in the i th bin, σ_i is the statistical uncertainty on the number of events in the i th bin of the true spectrum, (θ_{grid}) is the set of flux parameters

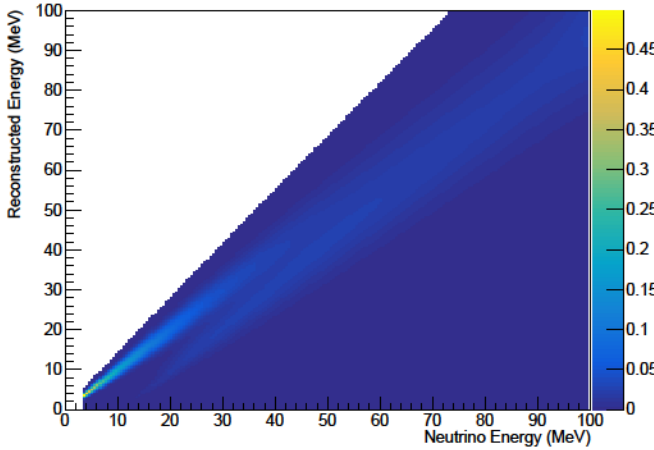


FIG. 2. SNOwGLoBES smearing matrix made with MARLEY modeling and 10% Gaussian-smeared reconstructed energy. An energy column contains the reconstructed energy distribution for neutrino-argon events at a given true neutrino energy.

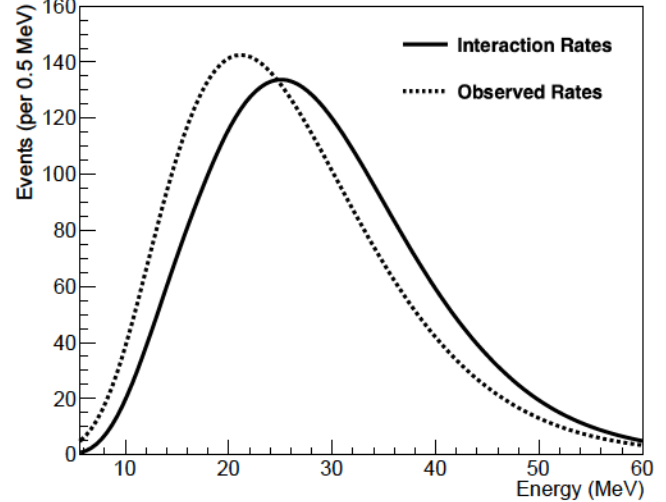


FIG. 3. Interacted and observed event rates calculated using SNOwGLoBES for ν_e - ^{40}Ar interactions in the proposed DUNE far detector. The post-smearing efficiency model imposed a sharp cut at 5 MeV onto the observed rates.

used to generate a reconstructed energy spectrum in the grid, and $(\alpha^0, \langle E_\nu \rangle^0, \varepsilon^0)$ are the flux parameters used to generate the true spectrum. We assume statistics corresponding to the approximately expected flux for a core collapse at 10 kpc.

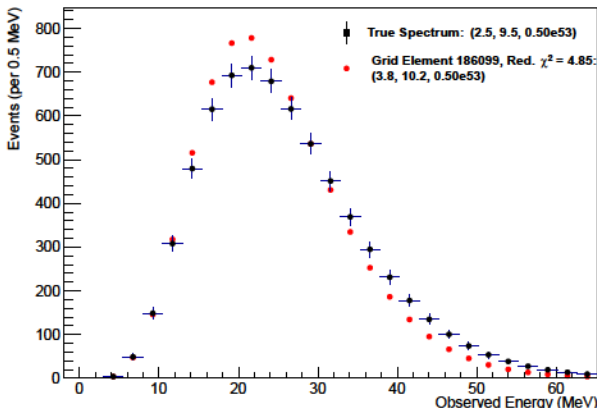


FIG. 4. Event rates calculated using SNOwGLoBES for a true spectrum with initial fluence parameters $(\alpha^0, \langle E_\nu \rangle^0, \varepsilon^0) = (2.5, 9.5 \text{ MeV}, 5 \times 10^{52} \text{ ergs})$ and an example grid element with fluence parameters $(\alpha^0, \langle E_\nu \rangle^0, \varepsilon^0) = (3.8, 10.2 \text{ MeV}, 5 \times 10^{52} \text{ ergs})$ and reduced $\chi^2 = 4.85$ based on Eq. 6. The error bars are statistical.

Figure 4 shows an example comparison of a true spectrum against one arbitrary grid element. Both spectra are represented by Asimov data sets; the error bars of the true spectrum are derived from the Poisson distribution. The true spectrum represents the predicted data that DUNE would observe during a supernova burst.

The collection of χ^2 values for each of the grid elements is used to determine the measurement uncertainty of the pinched-thermal parameters. We consider uncertainty regions in 2D parameter spaces $(\langle E_\nu \rangle, \alpha)$, $(\langle E_\nu \rangle, \varepsilon)$, and (α, ε) , where the smallest χ^2 is determined by profiling over the third parameter. We determine the approximate “sensitivity regions” by placing a cut of $\chi^2 - \chi_{\min}^2 = 4.61$ corresponding to a 90% confidence level for two free parameters [33][34]. A sensitivity region is equivalent to the Asimov confidence region for a perfect prediction [35].

Figure 5 shows sensitivity regions in $(\langle E_\nu \rangle, \varepsilon)$ space for three different supernova distances; the number of events scales with the supernova distance, meaning the regions will grow larger for a more distant supernova.

E. Figure of merit for forward fitting

We developed a figure of merit as a proxy for the systematic error due to the cross section uncertainty, where the figure of merit describes the best-fit measurement and characterizes DUNE’s expected sensitivity to the supernova flux parameters. The figure of merit B_x is defined as the fractional bias on the measurement of a parameter x obtained from the fitting procedure:

$$B_x \equiv \frac{x^{\text{b.f.}} - x^0}{x^0}. \quad (7)$$

The figure of merit depends on the best-fit value $x^{\text{b.f.}}$ and true value x^0 of $x \in \{\alpha, \langle E_\nu \rangle, \varepsilon\}$, where here we express $\langle E_\nu \rangle$ in MeV and ε in ergs.

For the studies presented in this paper, we define all of our grids using the same range of α and $\langle E_\nu \rangle$ values.

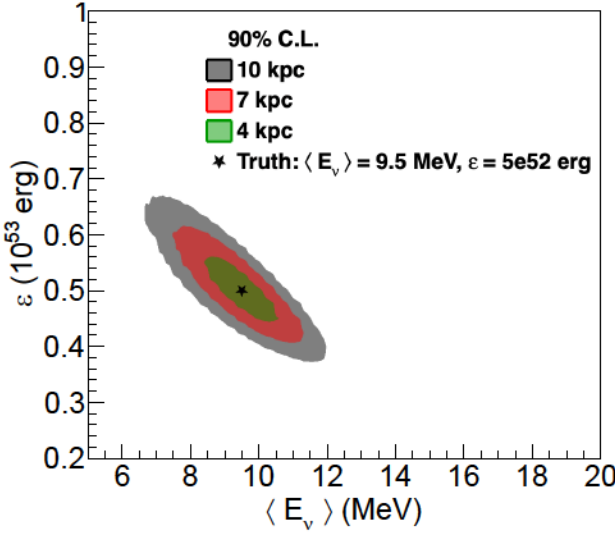


FIG. 5. Sensitivity regions in $(\langle E_\nu \rangle, \varepsilon)$ space for three different supernova distances. These regions were generated from the smearing matrix shown in Fig. 2, a cross section model from MARLEY [31], and a step efficiency function with a 5 MeV detection threshold.

The allowed ranges are defined using the ν_e truth values $(\alpha^0, \langle E_\nu \rangle^0, \varepsilon^0) = (2.5, 9.5, 5 \times 10^{52})$ and the following bounds for reasonable α and $\langle E_\nu \rangle$ values are taken from Ref. [25]:

- $\alpha \in [0.1, 7.0]$ with 0.1 spacing, corresponding to fractional bias values $B_\alpha \in [-0.96, 1.8]$
- $\langle E_\nu \rangle \in [5.0, 20.0]$ with 0.1 spacing, corresponding to fractional bias values $B_{\langle E_\nu \rangle} \in [-0.47, 1.10]$

For the ε parameter, Ref. [25] defined a reasonable range of $[2 \times 10^{52}, 1 \times 10^{53}]$ with 2.5×10^{51} spacing, corresponding to bias values $B_\varepsilon \in [-0.6, 1.0]$. We used this range for the study outlined in Sec. III B. However, for the studies outlined in Secs. III C and III E, this range was insufficient to study the totality of the cross-section space covered by the various $\nu_e - {}^{40}\text{Ar}$ scattering models used in this paper. Therefore, we used the following (more conservative) range of $\varepsilon \in [1.0 \times 10^{51}, 1.0 \times 10^{54}]$ over several grids with spacings ranging from 2×10^{51} to 5×10^{52} ; the total range of ε values corresponds to bias values $B_\varepsilon \in [-1.0, 19.0]$.

F. Study assumptions

Here we summarize the assumptions used for the studies presented in this paper:

- All neutrino species contribute to the pinched-thermal flux, where the true parameters for each flavor (before any flavor transition) are defined below [25].

$$\begin{aligned} &-\nu_e \text{ flux: } (\alpha^0, \langle E_\nu \rangle^0, \varepsilon^0) = (2.5, 9.5, 5 \times 10^{52}) \\ &-\bar{\nu}_e \text{ flux: } (\alpha^0, \langle E_\nu \rangle^0, \varepsilon^0) = (2.5, 12.0, 5 \times 10^{52}) \\ &-\nu_x \equiv \nu_\mu, \nu_\tau, \bar{\nu}_\mu, \bar{\nu}_\tau \\ &\text{flux: } (\alpha^0, \langle E_\nu \rangle^0, \varepsilon^0) = (2.5, 15.6, 5 \times 10^{52}) \end{aligned}$$

- A pure pinched-thermal supernova flux.
- Normal mass ordering with standard MSW transition effects implemented using Eq. 5; no “collective” effects, spectral swaps or non-standard flavor transition effects.
- A supernova distance of 10 kpc with no distance uncertainty.
- Event rates integrated over a supernova burst lasting 10 seconds.
- Only charged-current $\nu_e - {}^{40}\text{Ar}$ interactions in the simulated observed signal.
- SNOwGLoBES smearing matrix made with MARLEY modeling [31] and 10% Gaussian smearing.
- Post-smearing efficiencies in SNOwGLoBES of 100% efficiency above a 5 MeV detection threshold.

G. Additional information to reproduce the results

The studies in this paper used the following software:

- SNOwGLoBES 1.2 [28]
- MARLEY 1.2.0 [31]
- ROOT 6.20 [36]

The studies rely heavily on simulated supernova event rates calculated with SNOwGLoBES. Instructions for how to produce single event rate files, along with grids of flux files, are included in the SNOwGLoBES software package. We used the MARLEY event generator to simulate $\nu_e - {}^{40}\text{Ar}$ interactions while creating a smearing matrix for usage in SNOwGLoBES. The smearing matrix was created using SNOwGLoBES with 10% Gaussian smearing applied. The forward-fitting algorithm and studies were conducted using ROOT; the forward-fitting algorithm is publicly available on GitHub at <https://github.com/erinecon/forward-fitting>.

III. CROSS-SECTION STUDIES

With the forward-fitting algorithm implemented to measure the spectral parameters, construct sensitivity regions, and calculate the bias figure of merit, we studied how the choice of $\nu_e - {}^{40}\text{Ar}$ cross-section model could impact a supernova neutrino measurement in DUNE. Understanding systematic uncertainties and potential biases introduced by mismodeling of the cross section will be essential for a correct interpretation of any future core-collapse supernova observation.

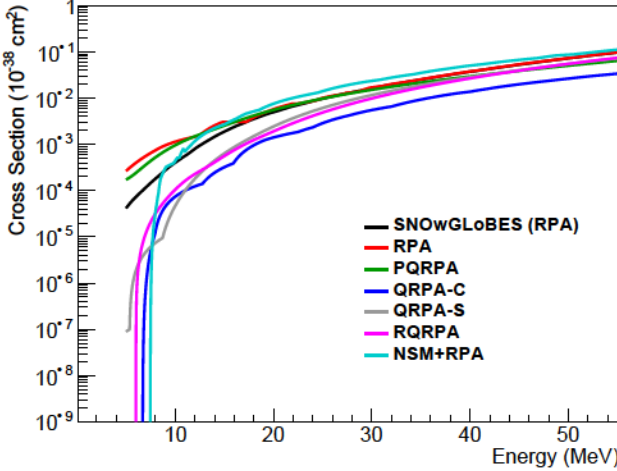


FIG. 6. Cross-section calculations for the $\nu_e - {}^{40}\text{Ar}$ interaction from Refs. [28], [37, 38], [39], [40], [41], [42], and [43]. The labels are explained in Table I. Note the log scale on the y-axis.

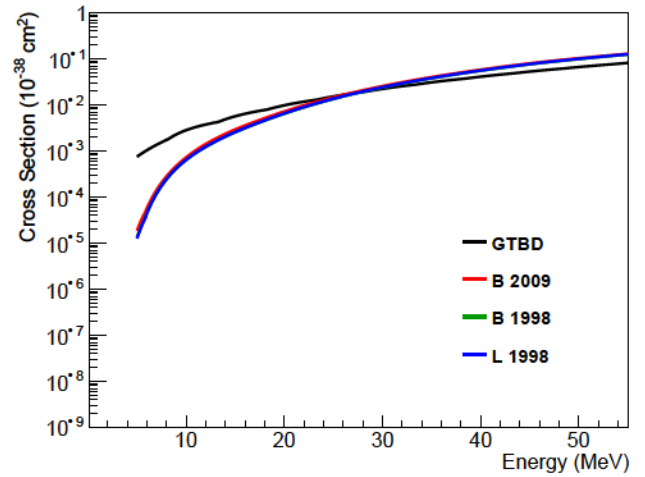


FIG. 7. Cross section calculations for the $\nu_e - {}^{40}\text{Ar}$ interaction from Refs. [30] and [44]. The labels are explained in Table I. The y-axis range is the same as Fig. 6.

A. Neutrino-argon cross section models

Many calculations of the $\nu_e - {}^{40}\text{Ar}$ cross section have emerged over time using various nuclear structure models. In the studies performed for this paper, twelve cross-section models are considered. Table I briefly summarizes the features of the models. Figures 6 and 7 show the total charged-current cross sections predicted by each of the models in the energy region of interest. The models were split into two plots for easier readability; the RPA models are all contained in Fig. 6, while the GTBD model and the cross-sections calculated by MARLEY are contained in Fig. 7.

The majority of these cross-section models are based on microscopic calculations using formalisms such as the Random Phase Approximation (RPA) or Quasiparticle RPA (QRPA). Under these approaches, collective states of nuclei are described using particle-hole (quasiparticle) excitations. The RPA-based calculations include contributions from forbidden (or high-multipole-order) nuclear transitions, which become especially important for neutrinos with $E_\nu > 50$ MeV. A hybrid microscopic calculation [40] in which the allowed (lowest-multipole-order, i.e., Fermi and Gamow-Teller transitions) contributions were computed using the nuclear shell model (NSM) and the forbidden contributions were treated using the RPA is also considered. Alternative macroscopic models like that in Ref. [44] use calculations based on the gross theory of beta decay (GTBD) that describe the global properties of allowed β -decay processes. The calculations from MARLEY [31] are partially data-driven and neglect forbidden nuclear transitions. A QRPA calculation is used by MARLEY at excitation energies where relevant data are not currently available.

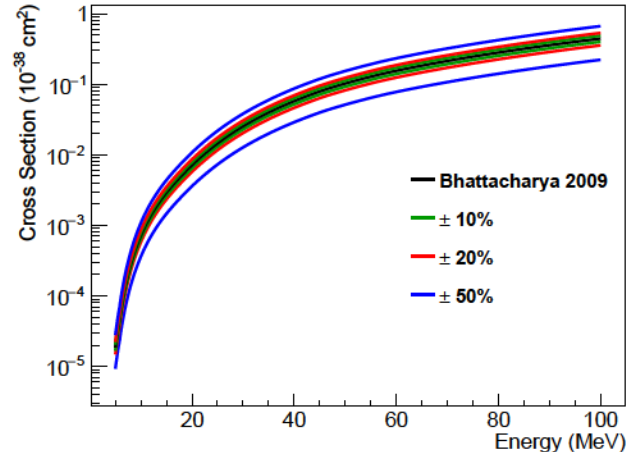


FIG. 8. $\nu_e - {}^{40}\text{Ar}$ cross section versus energy with various scaling factors applied. Ref. [30] provided the cross section model obtained from Bhattacharya (2009) data [49].

B. Cross section normalization uncertainty

As a first examination of the impact of cross-section uncertainties on the extraction of supernova flux parameters from a future DUNE data set, we consider model variations that involve the application of a constant overall scaling factor. These variations shift a plot of $\sigma(E_\nu)$ vertically while leaving the shape unchanged (see Fig. 8). We adopt as a reference model a cross section from MARLEY version 1.2.0 [30] [50].

The data-driven nuclear matrix elements in this model were obtained from a measurement of very forward (p, n) scattering reported in Ref. [49]. The unaltered reference

TABLE I. Brief features of $\nu_e - {}^{40}\text{Ar}$ cross-section models used in this work.

Cross section model	Model name	Comments
Default model implemented in SNOwGLoBES [28]	SNOwGLoBES or S	Based on RPA calculations for all multipole transitions up to $J^\pi = 4^\pm$.
Calculation by Martinez-Pinedo et al. [37, 38]	RPA	Based on RPA calculations including all the multipole transitions up to $J^\pi = 6^\pm$.
Calculation by M. Cheoun et al. [42]	QRPA-C	Based on QRPA calculations. The results are consistent with data from (p, n) scattering reactions and Gamow-Teller strengths.
Calculation by N. Paar et al. [39]	RQRPA	Based on a self-consistent theory framework for a relativistic nuclear energy density functional. The cross sections are including higher-order multipole transitions up to $J^\pi = 5^\pm$. The calculations provide a larger cross sections for ${}^{40}\text{Ar}$.
Calculation by A. Samana et al. [41]	PQRPA	Based on projected number QRPA including higher-order multipole transitions up to $J^\pi = 6^\pm$. These calculations were able to describe consistently the weak processes on ${}^{12}\text{C}$ [41] using a projection number particle procedure.
Calculation by A. Samana et al. [44, 45]	GTBD	Based on Gross Theory of Beta Decay, that describes global properties of β -decay processes. Refs. [44, 45] state that this model for heavy elements overestimated available data. Ref. [46] states that GTBD is less reliable compared to (p, n) scattering data.
Calculation by T. Suzuki and M. Honma [40]	NSMRPA or NSM+RPA	Based on a hybrid model calculation where partial cross sections for Fermi and Gamow-Teller transitions obtained using NSM, while other multipoles computed using RPA calculations.
MARLEY calculation based upon ${}^{40}\text{Ti}$ β decay data [31]	B 1998	Gamow-Teller matrix elements were extracted from a 1998 measurement by Bhattacharya et al. [47]. These are supplemented with QRPA matrix elements from Ref. [42] at high excitation energies.
MARLEY calculation based upon an alternative ${}^{40}\text{Ti}$ β decay data set [31]	L 1998	Gamow-Teller matrix elements were extracted from a 1998 measurement by Liu et al. [48]. These are supplemented with QRPA matrix elements from Ref. [42] at high excitation energies.
MARLEY calculation based upon (p, n) scattering data [31]	B 2009	Gamow-Teller matrix elements were extracted from a 2009 measurement by Bhattacharya et al. [49]. These are supplemented with QRPA matrix elements from Ref. [42] at high excitation energies.
Unpublished calculation by Samana and dos Santos [43]	QRPA-S	Based on QRPA calculations and using the same parametrization of present PQRPA, including higher-order multipole transitions up to $J^\pi = 6^\pm$.

model is used together with versions changed by factors of $\pm(5$ to $20)\%$ in 5% steps, $\pm 50\%$, and $+100\%$. This procedure yields a total of twelve unique cross section models, and those models generate different true spectra and grids that we used as input into the forward-fitting algorithm.

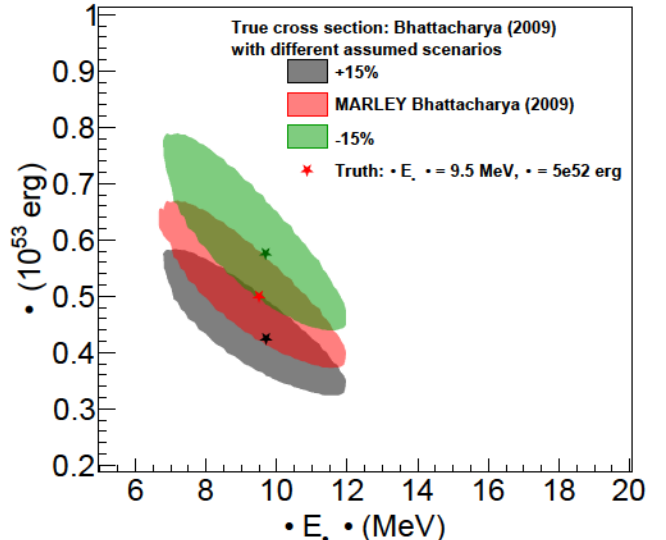


FIG. 9. Sensitivity regions (90% C.L.) for a 10 kpc supernova to study different combinations of assumed and true total cross section normalizations.

Figure 9 shows sensitivity regions for a 10 kpc supernova, the true scenario outlined in Sec. II F, and three different sets of assumptions. The sensitivity regions shift for changes in ; the cross section scaling factors affect the statistics and thus . The sensitivity regions shift vertically for change in cross-section normalization, with near-negligible shape change, as expected.

Figure 10 shows the bias in the best-fit parameter values for each possible combination of true cross-section model (i.e., the model used to simulate the fake data set) and assumed cross-section model (i.e., the model used to perform the parameter fits). The best fit within the grid bounds is determined, and that constraint can introduce an artificial bias to the best fit once a boundary is reached for one or more parameters. The results are shown separately for , , and . For each parameter, a two-dimensional histogram is plotted in which each bin represents a particular combination of cross-section models. The color of the bin represents the bias value, i.e., the fractional difference between the best-fit parameter value and its true value.

We first notice that the biases on and are relatively small unless the assumptions significantly differ from reality. If we assume an enhanced cross section (using positive scaling factors), the large mismatch in statistics causes an under-estimation. The difference in statistics forces the algorithm to select lower values. If we assume a reduced cross section (using negative scaling factors), we expect a lower event rate than we actually observe; thus the forward-fitting algorithm prefers higher values to compensate for the discrepancy. When the algorithm reaches a boundary (i.e., at the minimum or maximum value allowed), the biases in and will increase to compensate for spectral shape differences between the true spectrum and grid elements.

C. Physics content of the reference cross-section models

As mentioned above, Table I summarizes the features of the cross-section models used in this work. The models include those based on microscopic formalisms such as RPA [37, 38], QRPA [42], PQRPA [41], RQRPA [39], and NSM+RPA [40]; macroscopic models such as GTBD [44, 45]; and the MARLEY [31] phenomenological calculation based on a Monte Carlo approach. In the absence of any direct measurements of charged-current neutrino-argon scattering in the relevant energy range, experimental constraints on these theoretical approaches are poor. Nevertheless, we can make some general observations about the physics content of these models.

First, all of the microscopic models used here employ different residual interactions. These include the Skyrme interaction (including a spin-orbit term) in the RPA calculation, the Bonn CD potential in QRPA, the -interaction in PQRPA, the DDME2 relativistic nuclear energy density functional in RQRPA, and the monopole-

based-universal interaction (VMU) in NSM+RPA. The choice of residual interaction in each case was motivated by a successful description of some relevant experimental data, such as Gamow-Teller (GT) strengths, -decay rates, or energies of odd-odd neighboring nuclei.

Second, using a sufficiently large configuration space of nucleon states is important to prevent underestimation of the energy-dependent total cross section () as the neutrino energy rises. This is due in part to the increasing contribution of higher-order multipoles at high energies. The inclusive or total cross section as function of neutrino energy is a sum over all nuclear multipole states:

$$() = \left(\begin{array}{c} 0 \\ 1 \end{array} \right) + \left(\begin{array}{c} 0 \\ 1 \end{array} \right)^{\max} + \left(\begin{array}{c} 0 \\ 1 \end{array} \right) + \left(\begin{array}{c} 1 \\ 0 \end{array} \right) + \dots \quad (8)$$

Here, (\quad) is the cross section contribution due to multipole ; for example, see Eq. 2.25 in Ref. [51], or Eq. 3 in Ref. [40] for integration over neutrino angle. Usually, the contribution of the multipoles 0 and 1, allowed transitions, are the most important below neutrino energies of 50 MeV. Previous work with PQRPA and RQRPA on () reactions on C has examined the variation of () as a function of the space of single particle energies and the chosen value of the multipole cutoff \max [51]. It was found that the magnitudes of the resulting cross sections were close to the sum-rule limit at low energies but significantly smaller than this limit at high energies. As the size of the configuration space is augmented, () increases steadily, particularly for () energies greater than 200 MeV. Convergence is achieved when the configuration space and multipole cutoff (\max) are both chosen to be sufficiently large [51].

A few words are necessary for the GTBD result. This is a parametric model for -decay rates, which includes statistical arguments in a phenomenological way through a convolution between the independent particle model - amplitude and the level density of the Fermi gas model corrected to take into account shell effects. The GTBD calculation considers only the contributions of allowed transitions, (0) and (1), with a realistic description of the energy of the GT resonance peak [44, 45].

Third, some calculations use an effective (or *quenched*) value of the nucleon axial-vector coupling constant for which its bare value $A_A = 1.2756$ from the experimental data [33] is multiplied by a factor of around 0.8. There is still a lack of consensus in the nuclear physics community about whether this quenching is needed. For the family of models considered in this paper, the RPA calculations do not use a re-normalization of A_A [38], while the RQRPA model used $A_A = 1$. The PQRPA calculations also adopted $A_A = 1$ to be consistent with comparisons of 2s1d and 2p1f shell- model predictions with measured allowed -decay rates [51] and with recent double beta decay calculations. The QRPA calculations reported in Ref. [42] use a universal quenching factor $= A_{A_{\text{eff}}} / A_A = 0.74$ to reproduce measured

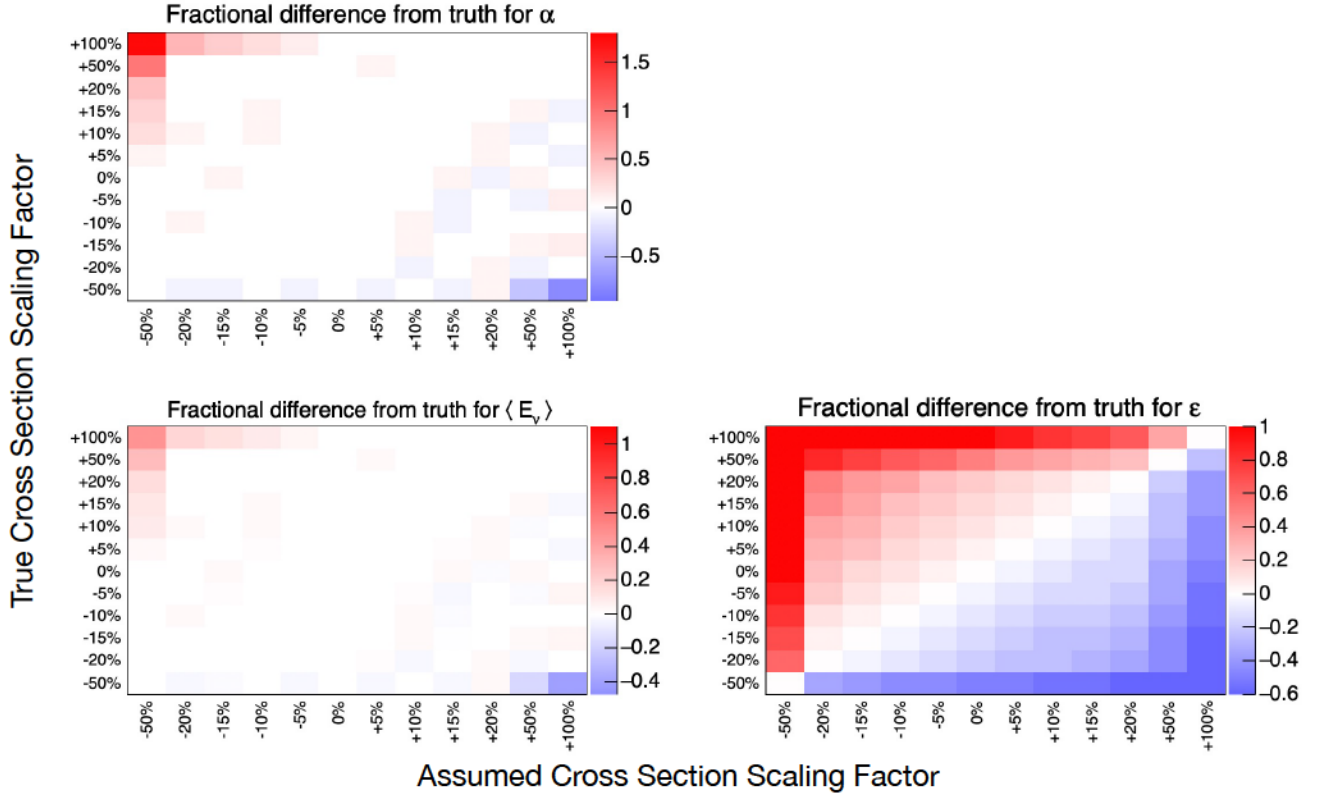


FIG. 10. 2D fractional difference plots to study effects produced by normalization uncertainties on the total cross section.

GT strength distributions. The NSM+RPA calculations within the VMU potential used a similar quenching factor $f_q = 0.775$ with $g_A = 1.263$. This choice enabled the NSM+RPA model to describe the experimental cumulative sum of the GT strength rather well. On the other hand, recent studies on variations of g_A in the GTBD have shown that best results for a set of 94 nuclei of interest are obtained with $g_A = 1$ [52]. The GT distribution used for the NSM+RPA calculation is shifted toward higher energy values with significantly smaller strengths for < 10 MeV neutrino energies, resulting in a characteristic cut-off at energies below about 8 MeV.

Despite the differences explored above, the main features of measured weak interaction observables, such as β -decay strengths and inclusive muon capture rates, are reasonably well described for multiple nuclei by the majority of the nuclear structure models considered herein. By incorporating these cross-section models into our SNOwGLoBES calculations, we studied the impact of variations in the shape of $\sigma(E_{\nu})$ on the simulated measurements of supernova neutrino flux parameters. Many of the cross section models required re-formatting with extra data-points for usage in SNOwGLoBES; appendix A provides more details on the interpolation procedure that was used. Figures 6 and 7 show that the cross-section models differ considerably and lead to a wide range of predictions for the supernova ν_e signal in

DUNE. Appendix B provides a table of the corresponding event rates as output by SNOwGLoBES.

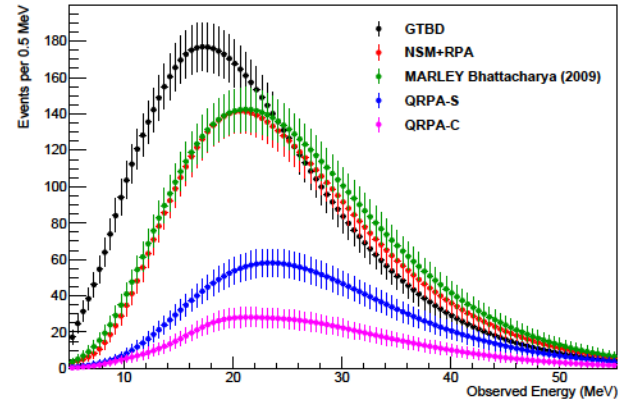


FIG. 11. SNOwGLoBES event rates for select cross-section calculations from Refs. [30, 40, 42–45]. Note that “QRPA-C” and “QRPA-S” contain the same type of calculation performed by different groups, with the former by M. Cheoun et al. [42] and the latter by Samana and dos Santos [43]. More details about the various models are provided in Table I. The error bars are statistical.

Figure 11 shows representative expected event rates in DUNE for the CC ν_e - ^{40}Ar absorption process and a su-

ernova at a distance of 10 kpc from Earth. The large differences in the cross-section model predictions at low neutrino energy translate to large variations in the plotted observed energy distributions. Apart from effects of cross-section mismodeling (which are considered in the next section), the expected statistical uncertainty on the event rate has a strong effect on the precision with which the supernova flux parameter values may be measured. The sensitivity regions shown in Fig. 12 are obtained by considering the statistical uncertainty and using the same cross-section model to generate the fake data and extract the results. The GTBD cross section model, which predicts 7770 ν_e CC events, results in the tightest constraints on the flux parameters. The QRPA-C model predicts 1383 events and thus provides the loosest constraints.

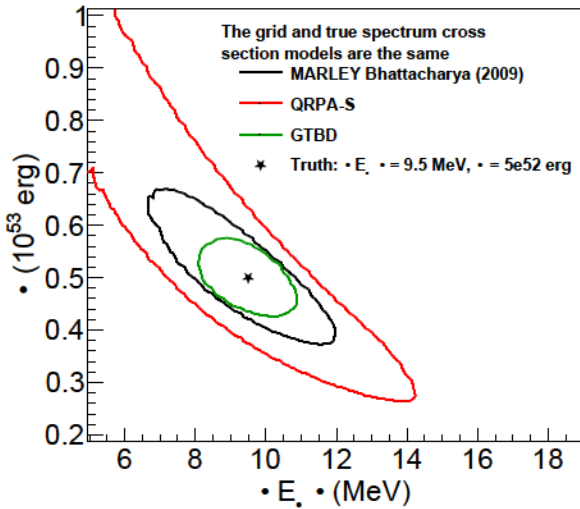


FIG. 12. Sensitivity regions (90% C.L.) in $(\langle E_\nu \rangle, \varepsilon)$ space generated from the cross-section models in Refs. [30, 43, 44]. Only statistical uncertainties are considered. In each case, the same cross-section model is used both to produce the fake data and to calculate the sensitivity region.

D. Combined cross-section normalization and shape uncertainty

To characterize the impact of using an inaccurate cross-section model to extract values of the supernova flux parameters, we consider scenarios in which different combinations of the theoretical models described in Sec. III C are used to (1) simulate a fake data set, and (2) perform fits of the flux parameters. Figure 13 displays the 2D bias plots for the different combinations of assumed and true total cross section models. A logarithmic color scale is used for ε due to the very large range of biases allowed for that parameter. In the 2D plots, the cross-section models are ordered along each histogram axis from smallest to largest expected number of events integrated over a neutrino energy range of [5, 15] MeV. Appendix B also contains the numerical values for the

expected event counts for each model in the [5, 15] MeV range.

Further insight into cross-section model effects on the extraction of supernova neutrino flux parameters can be gained from Fig. 14, which shows sensitivity regions computed based on a fake data set produced using the MARLEY B 2009 cross-section model. When supernova flux parameters are extracted using the same cross-section model (red sensitivity regions), the best-fit values (red stars) are identical to the true ones by construction. A small bias is seen when the extraction procedure is repeated using the MARLEY L 1998 model (black stars). However, the difference between the assumed (L 1998) and true (B 2009) cross sections is small enough that the gray sensitivity regions obtained from the new fit cover the true parameter values in all cases. A more problematic bias (green stars) is seen when the fit is repeated using the PQRPA model as the assumed cross section. In this case, the difference between the PRQPA and MARLEY B 2009 predictions is large enough to lead to green sensitivity regions which do not enclose the true results. This bias would need to be corrected in the context of a real analysis by introducing a cross-section-related systematic uncertainty to inflate the sensitivity regions. The significant corresponding loss of precision can be visually estimated from Fig. 14 by examining the degree to which the green sensitivity regions “miss” the red star that represents the true parameter values.

Some general trends were seen in the course of these fake data studies. If the cross-section model used for fitting gives higher values than the true one used to generate the fake data, then the fitting algorithm tends to overestimate α and $\langle E_\nu \rangle$ while underestimating ε . Because ε is directly proportional to the expected number of events, the best-fit value of ε is driven lower for fake data sets with low statistics.

E. Total cross section uncertainty envelope

The cross-section models considered above are not expected to produce results of equal quality in the energy region of interest for supernova neutrinos (see, e.g., the discussion in the supplemental materials from Ref. [46]), and furthermore, uncertainties are typically not available for them. As a means of assigning a theoretical uncertainty which neglects implausibly extreme variations, we consider the spread between three cross-section predictions: the partially data-driven MARLEY models [30], the NSM+RPA calculation [40], and the QRPA-S calculation [43]. In the absence of a direct measurement of the capture process on argon, we selected this subset of the available models based upon purely a priori considerations. Predictions from our chosen subset of cross-section models are shown in Fig. 15. An uncertainty envelope defined as the range between the minimum and maximum cross-section predictions from this subset of models is also shown as the crosshatched region. Predicted supernova neutrino event rates in DUNE for each of the models used to define the envelope are displayed in Fig. 17.

With a restricted range of cross-section variations defined in this way, we repeated our fake data studies using a new family of toy cross section models. The lower (Min) and upper (Max) bounds of the uncertainty envelope were treated as two of the new models, and the MARLEY B 2009 cross section [31] was treated as a midpoint. We further define four additional toy models in which three of the models attempt to cover the lower half of the envelope. The first toy model (“Lower bound toy model 1”) is an average between the MARLEY B 2009 cross section and the lower (Min) bound. The second toy model (“Lower bound toy model 2”) is defined as the average between the first toy model and the MARLEY B 2009 cross section. Finally, the third toy model (“Lower bound toy model 3”) is defined as the average between the first toy model and the lower (Min) bound. The complete set of toy cross section models is shown in Fig. 16. Note that the two “kinks” in the Min model are artifacts from linear interpolations of the NSM+RPA [40] and QRPA-S [43] models, respectively.

Figure 18 shows the 2D fractional difference plots for the toy cross section models within the uncertainty envelope. When compared to Fig. 13, the biases are less extreme for all three parameters. Similar to the previous fake data studies, extraction of best-fit values for θ and

δ is less affected by cross-section mismodeling while estimation of ϕ is impacted the most. Also similar to the previous studies, assuming a cross-section higher than the true one leads to an underestimation of ϕ . Example sensitivity regions are shown in Fig. 19 using several assumed cross sections for fake data generated using the MARLEY B 2009 model. In this case, the black star represents the true parameter values. The observed biases are still significant for θ but relatively modest for the other supernova flux parameters.

IV. DISCUSSION

A proper interpretation of a DUNE supernova neutrino data set will require a good understanding of neutrino-argon scattering cross sections in the tens of MeV regime. Since direct measurements of the dominant charged-current absorption process on argon are currently unavailable, our present consideration of cross-section uncertainties necessarily relies on calculations available in the theoretical literature. Furthermore, because few published calculations of observables beyond energy-dependent total cross sections () are available for CC - Ar scattering, we focus entirely upon variations to the total cross section. For the studies reported here, the remaining aspects of the interaction modeling needed to connect the true neutrino energy to the observed energy distribution in DUNE are provided by the MARLEY event generator, which currently implements the only realistic predictions of complete final states for low-energy CC neutrino-argon scattering. We expect the theoretical uncertainties on these additional modeling details to be significant, and future work will be needed to reliably quantify them.

To examine the impact of total cross-section mismodeling on the interpretation of DUNE supernova neutrino data, we employed three strategies for model variations: applying a constant scaling factor to the MARLEY B 2009 model (Sec. III B), considering the full range of a variety of cross-section predictions (Sec. III D), and defining an uncertainty envelope based on the spread of a subset of selected predictions (Sec. III E). Beyond the phenomenological models available in MARLEY, the theoretical calculations that we reviewed and employed for the latter two strategies included the global GTBD treatment and microscopic evaluations such as the QRPA, PQRPA, NSM, and hybrid approaches. All of these models have significant differences coming from the description of nuclear correlations, the residual interaction, and the value of the nucleon axial-vector coupling. Nevertheless, these models reasonably describe the main features of measured weak interaction observables such as β -decay strengths and inclusive muon capture rates.

For all three strategies, the cross-section model variations were applied to toy measurements of supernova neutrino flux parameters performed using fake data sets produced using the SNOWGLOBES framework. Different combinations of true and assumed cross section models (used to create the fake data and interpret the toy measurement results, respectively) were employed, and the impact on the extracted values of the flux parameters was assessed.

Table II provides a high-level summary of the conclusions from our fake data studies. For each of the three supernova neutrino flux parameters that we considered, an uncertainty on the total CC neutrino-argon cross-section of -50/+100% and $\sim 20\%$ is translated into a corresponding range of observed biases on the best-fit parameter value extracted from the toy measurements. The val-

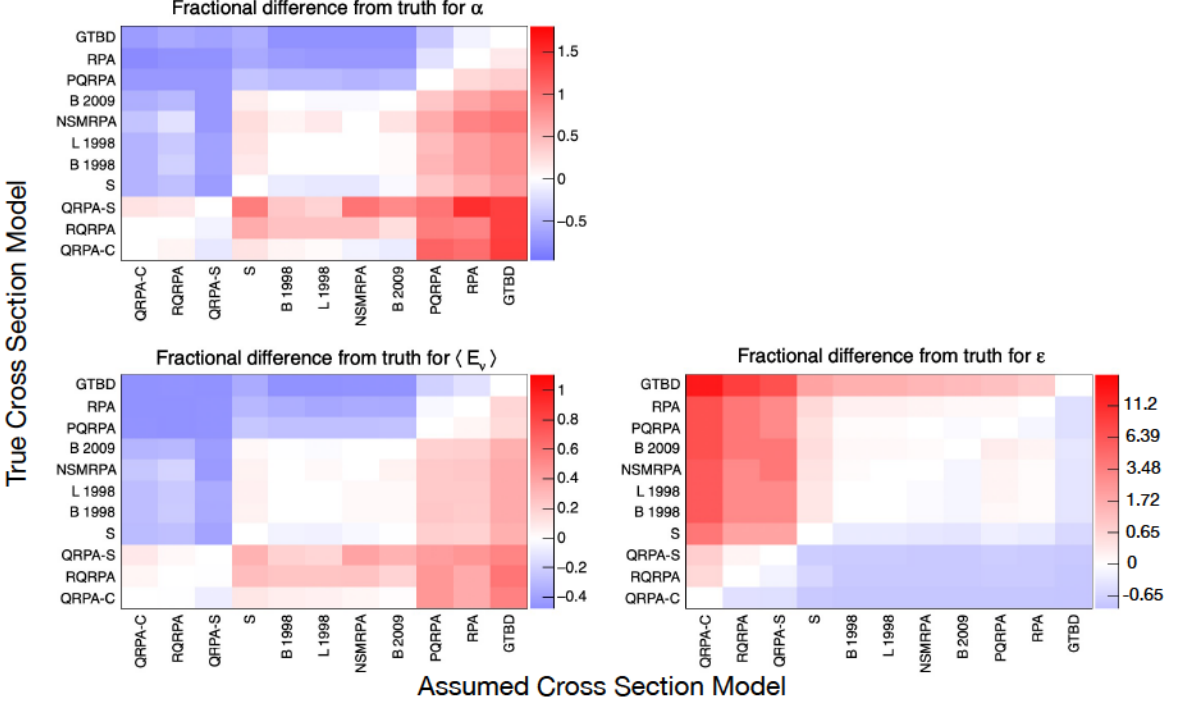


FIG. 13. 2D fractional difference plots to study effects produced by different cross section models. Note that “S” stands for the cross section model implemented into SNOwGLoBES [28]. Also note that the ϵ color-scale is log to account for the wide range of values. The number scale shows the raw fractional difference values to conform with the α and $\langle E_\nu \rangle$ plots.

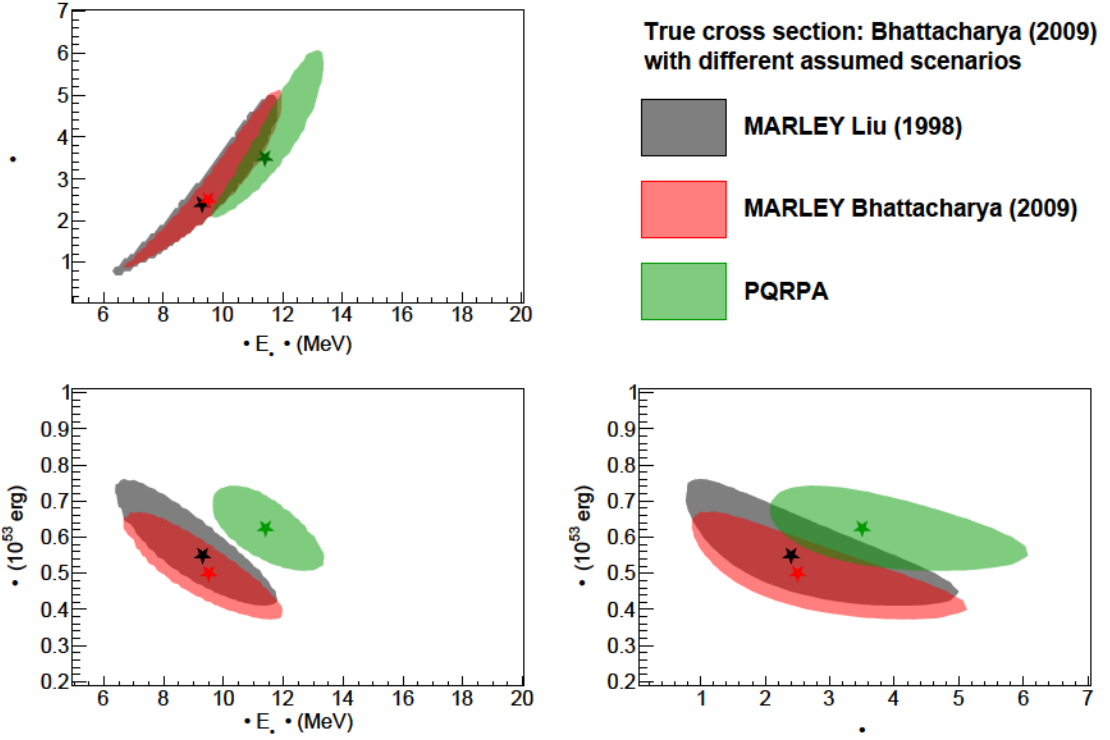


FIG. 14. Sensitivity regions (90% C.L.) calculated with different assumed cross-section models for a fake data set generated using the MARLEY B 2009 model. The stars mark the best-fit measurements from the fitting algorithm. The red stars also indicate the true parameter values, i.e., when the assumed cross section model is identical to the true model.

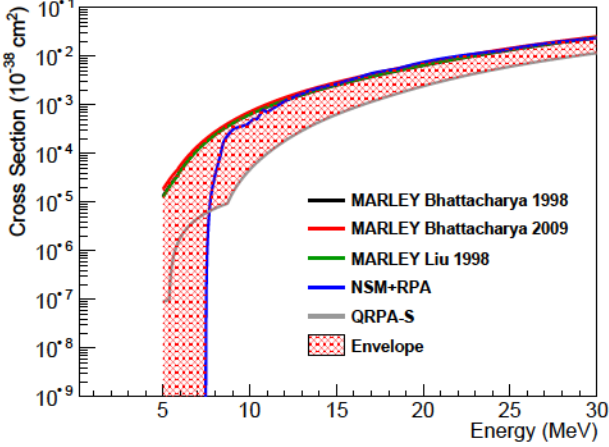


FIG. 15. Total cross section predictions for the $\nu_e - {}^{40}\text{Ar}$ interaction from the selected subset of models discussed in Section III E. The shaded region represents the adopted uncertainty envelope based on the spread of these models.

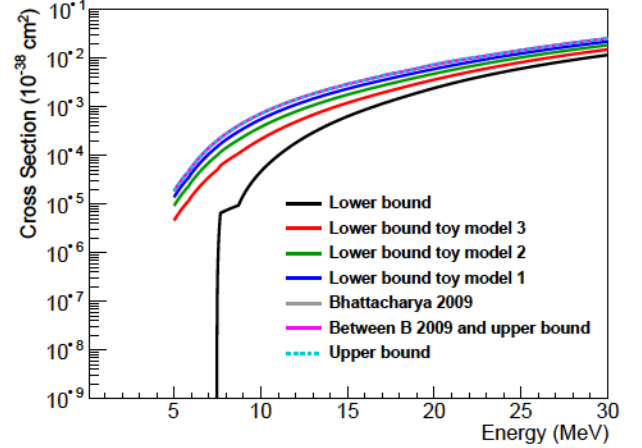


FIG. 16. Toy total cross-section models for the $\nu_e - {}^{40}\text{Ar}$ interaction covering portions of the uncertainty envelope shown in Fig. 15.

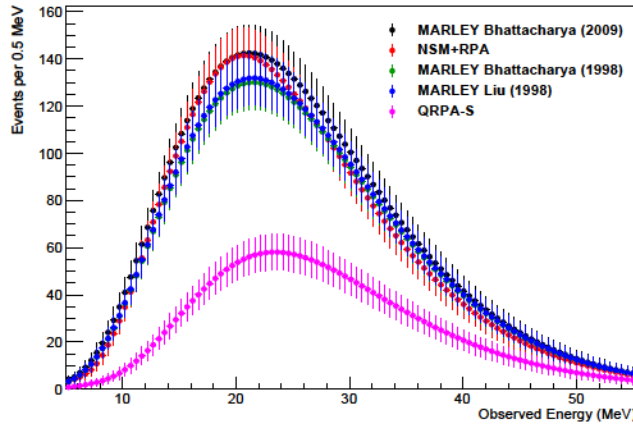


FIG. 17. SNOwGLoBES event rates for the selected cross-section calculations discussed in the text. The error bars are statistical.

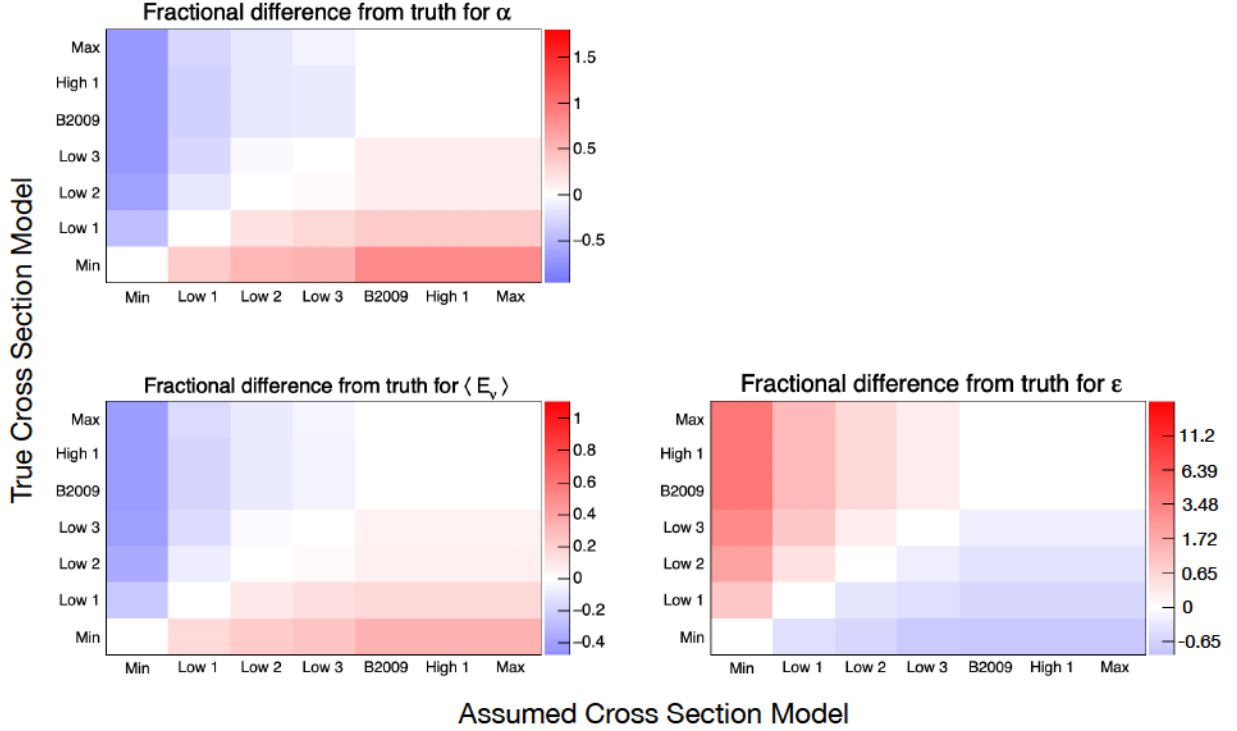


FIG. 18. 2D fractional difference plots to study effects produced by toy models within the cross section uncertainty envelope discussed in Section III E.

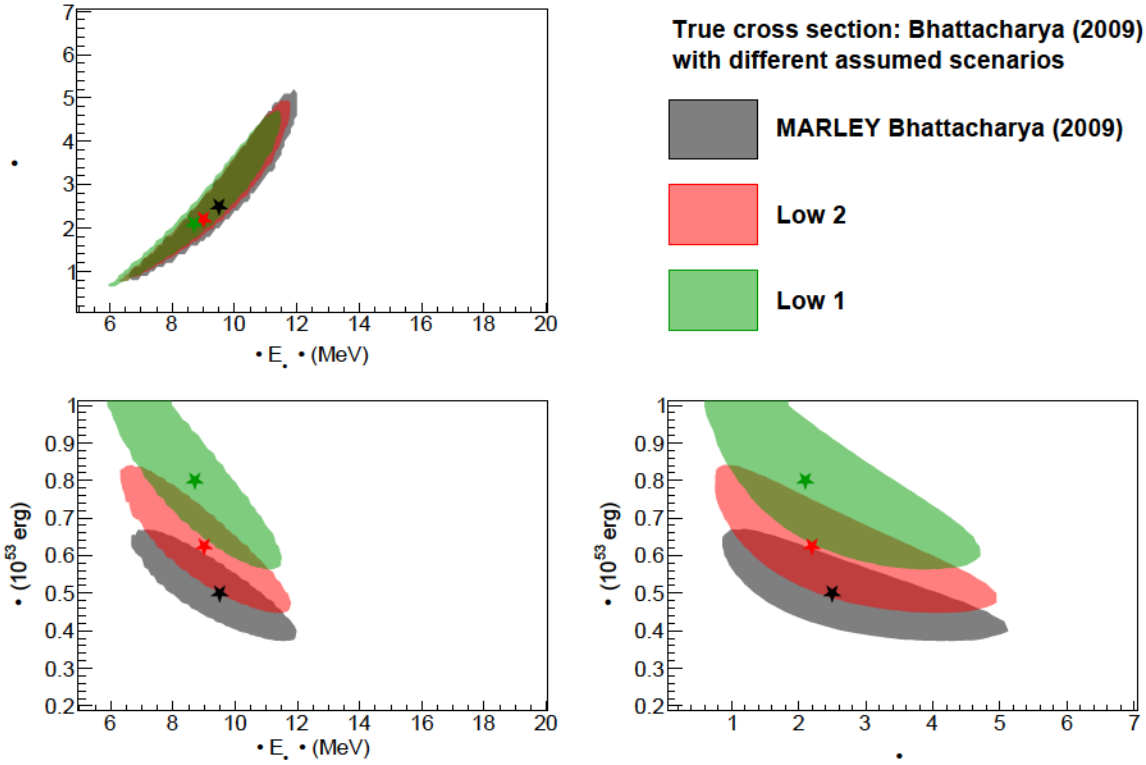


FIG. 19. Sensitivity regions (90% C.L.) with different combinations of assumed and true cross section models. Two of the models are toy models generated from the midpoint (B 2009) and minimum cross section values from the set of selected models. The stars mark the best-fit values from the fitting algorithm. The black stars also represent the true parameter values.

ues of the bias were read directly off the 2D fractional difference plots. For the -50/+100% combination, the forward-fitting algorithm reached the most extreme allowed values of , causing the biases in and to increase in an attempt to compensate for the spectral shape differences between the true spectrum and grid elements.

For total cross section known at about the 20% level, bias on best-fit and is in the 3-8% range. Achieving less than 10% bias on the best-fit value of requires the cross section to be known to about 5%. These requirements may be somewhat relaxed in light of possible constraints from simultaneous observations of the supernova by other detectors, which we do not consider here. On the other hand, more stringent requirements may ultimately be needed when additional interaction modeling uncertainties (beyond those on the total cross section) are fully taken into account.

While we are optimistic that the theoretical understanding of low-energy neutrino-argon cross sections will continue to improve, there is no substitute for actually measuring the cross sections with a well-characterized neutrino flux. Pions decaying at rest represent a near-ideal source of neutrinos for such measurements. Decays of produce monochromatic on a short timescale, plus and from delayed decay of the stopped daughter muon on a 2.2 s timescale. The spectrum and timing are very well understood. The neutrino energies extend to 52 MeV, overlapping nicely with the supernova spectrum. It is also possible to study neutral-current argon inelastic events given the time structure of the beam. Spallation-based neutron beams such as the Spallation Neutron Source at Oak Ridge National Laboratory [53], the Lujan Neutron Science Center at Los Alamos National Laboratory [54], the J-PARC Spallation Neutron Source [55], and the future European Spallation Source [56] (currently under construction) are intense sources of pion decay-at-rest neutrinos. Measurements of these neutrinos may also be possible at high-energy physics facilities including the Large Hadron Collider beam dump [57] and the meson decay-in-flight neutrino beams at Fermilab [58].

Future direct measurements of CC -argon cross sections using a pion decay-at-rest source could pursue several distinct observables to better constrain interaction

TABLE II. Parameter biases caused by normalization uncertainties on the total cross section.

uncertainty	Parameter	Measurement bias
-50/+100%		-80% to +176%
		-41.1% to +47.4%
		-60% to +100%
20%		0% to +8%
		-3% to 0%
		-45% to +50%

modeling uncertainties for the DUNE supernova neutrino program. The most straightforward of these (and most directly relevant to the specific uncertainties considered in this paper) would be an inclusive total cross section averaged over the flux (ν) from decays at rest:

$$\frac{(\nu) (\nu)}{(\nu)} \quad (9)$$

where is the muon mass and

$$(\nu) = (\nu^2) \quad (10)$$

Measurements of both and a differential cross section as a function of the total visible energy would likely be obtainable with a suitably large (several-ton-scale) argon detector. As an example, 5-10% statistical uncertainty on the total cross section could be obtained in a few years with a ton-scale detector a few tens of meters from the Spallation Neutron Source.

The fine spatial resolution of a LArTPC detector would potentially allow for more detailed measurements. In particular, topological separation between the outgoing electron and -rays emitted due to neutrino-induced nuclear de-excitations could allow separate measurements of differential distributions for both particle species. Recent studies (e.g., Ref. [59]) suggest that such a separation would be feasible, and a successful implementation would yield a rich data set: the inclusive electron energy and angular distributions are known to be sensitive to the modeling of forbidden contributions to the cross section [60], while the -rays would provide a helpful constraint on de-excitation modeling and, in principle, the opportunity to measure partial cross sections for specific nuclear transitions. Measuring the neutrino angular distribution is particularly important for supernova pointing measurements relevant for prompt multi-messenger astrophysics [12, 61].

An especially impactful but highly challenging measurement would involve the detection of final-state neutrons produced by CC -argon interactions. Missing energy attributable to these neutrons is expected to have a significant impact on neutrino energy reconstruction at supernova energies [30], and the modeling needed to account for it is complicated and poorly constrained by experimental data. In the absence of any new experimental techniques to increase the sensitivity of argon-based detectors to neutrons at and below MeV energies, external instrumentation designed to capture and detect escaping neutrons would likely be the only means of attempting such a measurement.

V. CONCLUSION

A possible future observation by DUNE of neutrinos from a core-collapse supernova would represent a rare

and valuable scientific opportunity. In particular, the unique sensitivity of DUNE’s LArTPC detectors to the component of the supernova neutrino flux would be highly complementary to other current and anticipated large neutrino experiments. In the studies reported in this paper, we have examined the effects of cross-section modeling uncertainties on a simulated analysis of supernova neutrinos in DUNE.

Significant experimental and theoretical challenges remain before a precise understanding of tens of MeV neutrino-argon scattering can be achieved. Nevertheless, pursuing this understanding will be essential to maximize the discovery potential from a core-collapse supernova observation (and a potentially broader program of low-energy physics) in DUNE. We hope that the initial studies of neutrino-argon interaction modeling uncertainties reported here may serve as a useful foundation for the more comprehensive investigations that will be required in the future.

VI. ACKNOWLEDGEMENTS

This document was prepared by the DUNE collaboration using the resources of the Fermi National Accelerator Laboratory (Fermilab), a U.S. Department of Energy, Office of Science, HEP User Facility. Fermilab is managed by Fermi Research Alliance, LLC (FRA), acting under Contract No. DE-AC02-07CH11359.

This work was supported by CNPq, FAPERJ, FAPEG and FAPESP, Brazil; CFI, IPP and NSERC, Canada; CERN; MŠMT, Czech Republic; ERDF, H2020-EU and MSCA, European Union; CNRS/IN2P3 and CEA, France; INFN, Italy; FCT, Portugal; NRF, South Korea; CAM, Fundación “La Caixa”, Junta de Andalucía-FEDER, MICINN, and Xunta de Galicia, Spain; SERI and SNSF, Switzerland; TÜBİTAK, Turkey; The Royal Society and UKRI/STFC, United Kingdom; DOE and NSF, United States of America.

This work was also supported by FAPESB T.O. PIE 0013/2016 and UESC/PROPP 0010299-61.

Appendix A: Interpolation/extrapolation methods used on cross section models

In order to study the measurement biases introduced by the cross-section modeling, we obtained numerical tables of model predictions for the total charged-current

- Ar cross section (see Table I). SNOWGLOBES requires 1001 data points in a cross section file for neutrino energies between 5-100 MeV. While some of the models of interest are already available within SNOWGLOBES (including its default cross section model, along with some MARLEY cross section models from Ref. [30]), input files for the other models required extra preparation to conform to the requirements of the SNOWGLOBES format.

Table III summarizes the interpolation and extrapolation methods used for the various models. Excluding the cross section models already available within SNOWGLOBES, all models required interpolation between their tabulated data points to obtain cross section values at intermediate neutrino energies. For models which were tabulated over the entire energy range of interest, either a cubic spline or a linear spline was used to interpolate between the given data points. A cubic spline was generally preferred, but the linear spline was used in cases where the cubic spline caused unphysical fluctuations in the interpolated total cross section.

The available cross-section tables for some models did not cover the entire 5–100 MeV energy range required by SNOWGLOBES. In such cases, extrapolation techniques were used to extend the existing predictions. The models from Refs. [37, 38, 40, 44, 45] required extrapolation down to 5 MeV, while the model from Ref. [42] required extrapolation down to 5 MeV and up to 100 MeV. All of the extrapolations used to prepare the SNOWGLOBES input files employed a quadratic fit of the form

$$() = () \quad (A1)$$

where and are the free parameters used for fitting. All extrapolation fits used five data points.

In the fits for low energies, (which has units of MeV) holds special significance as the “endpoint” of the cross section model because it is the minimum of the quadratic function. For ≈ 5 MeV, the fit would introduce unphysical behavior into the model in the form of an increasing cross section as the neutrino energy approaches 5 MeV from above. To prevent this behavior, the total cross section (≈ 5 MeV) was zeroed out for all energies whenever ≈ 5 MeV. The same quadratic functional form was also fit to the last five data points of the model from Ref. [42] to extrapolate up to 100 MeV. In this case, the low- and high-energy fits were handled independently. In order to avoid discontinuities between the interpolation and extrapolation methods, the fits performed at low (high) neutrino energy were required to pass through the first (last) tabulated data point for the cross-section model of interest. Fig. 20 shows the cross section model from Refs. [44, 45] as an example of the interpolation between points (in this case, with a linear spline) as well as an extrapolation to low energies.

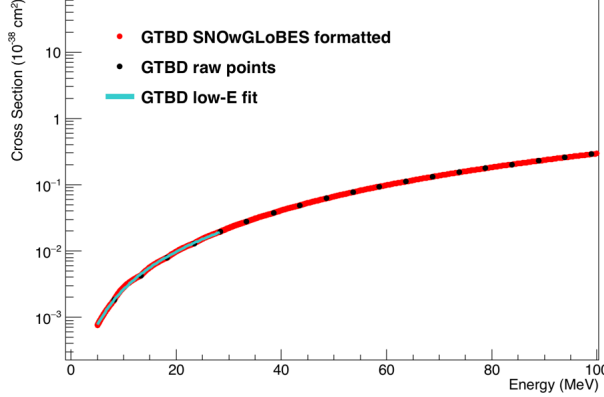


FIG. 20. Cross section model from Ref. [44, 45] with the interpolation (with a linear spline) and extrapolation (using a quadratic fit) shown. See Table III for the quadratic fit parameters for the low-energy fit.

TABLE III. Table summarizing the interpolation and extrapolation methods performed on the various cross section models to format them for usage in SNOwGLoBES [28]. Parameters from the quadratic fits described in the text are also given when extrapolation was used.

Cross section model	Interpolation method used	Extrapolation method used
SNOwGLoBES [28]	N/A	N/A
RPA [37, 38]	Linear spline	Low-energy quadratic fit: e-
QRPA-C [42]	Linear spline	Low-energy quadratic fit: e- ; for all energy values below MeV, the cross section was set to zero.
GTBD [44, 45]	Linear spline	High-energy quadratic fit: e-
NSM+RPA [40]	Linear spline	Low-energy quadratic fit: e- ; for all energy values below MeV, the cross section was set to zero.
QRPA-S [43]	Linear spline	N/A
RQRPA [39]	Cubic spline	N/A
PQRPA [41]	Cubic spline	N/A
B 1998 [31]	Cubic spline	N/A
B 2009 [31]	Cubic spline	N/A
L 2009 [31]	Cubic spline	N/A

Appendix B: SNOwGLoBES event rates for different cross section models

TABLE IV. SNOwGLoBES estimated number of CC events in the DUNE far detectors for pinched-thermal flux parameters for the flavor, a 10-kpc supernova, and assuming NMO and MSW oscillations via Equation 5.

Cross section model	Number of CC events	Number of CC events between MeV
QRPA-C [42]	1383	134
RQRPA [39]	2243	220
QRPA-S [43]	2791	243
SNOwGLoBES [28]	4486	624
B 1998 [31]	6307	874
L 1998 [31]	6390	883
NSM+RPA [40]	6391	897
B 2009 [31]	6852	988
PQRPA [41]	4562	909
RPA [37, 38]	5064	998
GTBD [44, 45]	7770	2070

Appendix C: Interpolating sensitivity regions

To keep computation time reasonable, the algorithm used to compute flux parameter sensitivity regions (see Sec. II D) uses a limited number of elements in the grid of reference () values. The limited number of grid elements leads to unphysical jagged edges in plots of the 90% confidence contours used in this paper to estimate DUNE sensitivity regions for the supernova spectral parameters. To remove these artifacts from the sensitivity region plots, we developed an interpolation technique to smooth the contour edges. Each contour was stored as a two-dimensional histogram, where the weight in each bin was calculated as the minimum value obtained in that region of 2D flux parameter space. Bilinear interpolation [62] between histogram bins was then used to increase the number of bins along each axis to 1000. Example sensitivity regions for the MARLEY B 2009 model are

shown in Fig. 21 before (black) and after (blue) applying the smoothing procedure. The impact of the smoothing is most noticeable in the plots involving since the reference

grid is coarsest for that parameter. Specifically, the interpolated contours are slightly smaller than the original contours.

-
- [1] A core collapse leaving behind a black hole may not result in a visible supernova, but will still emit a bright burst of neutrinos.
- [2] J. F. Cherry, J. Carlson, A. Friedland, G. M. Fuller, and A. Vlasenko, *Phys. Rev. D* **87**, 085037 (2013).
- [3] J. F. Beacom, R. N. Boyd, and A. Mezzacappa, *Phys. Rev. D* **63**, 073011 (2001).
- [4] R. C. Schirato and G. M. Fuller, (2002), arXiv:astro-ph/0205390 [astro-ph].
- [5] F. Hanke, A. Marek, B. Müller, and H.-T. Janka, *The Astrophysical Journal* **755**, 138 (2012).
- [6] A. Friedland and A. Gruzinov, (2006), arXiv:astro-ph/0607244 [astro-ph].
- [7] R. M. Bionta *et al.*, *Phys. Rev. Lett.* **58**, 1494 (1987).
- [8] K. Hirata *et al.* (KAMIOKANDE-II), *Phys. Rev. Lett.* **58**, 1490 (1987).
- [9] E. N. Alekseev, L. N. Alekseeva, V. I. Volchenko, and I. V. Krivosheina, *JETP Lett.* **45**, 589 (1987).
- [10] M. Aglietta *et al.*, *Europhys. Lett.* **3**, 1315 (1987).
- [11] K. Scholberg, *Annu. Rev. Nucl. Part. Sci.* **62**, 81–103 (2012), arXiv:1205.6003 [astro-ph.IM].
- [12] B. Abi *et al.* (DUNE Collaboration), *Eur. Phys. J. C* **81**, 423 (2021), arXiv:2002.03005 [hep-ex].
- [13] D. Caratelli *et al.*, in *2022 Snowmass Summer Study* (2022) arXiv:2203.00740 [physics.ins-det].
- [14] If solar-neutrino flux is assumed known, one can in principle use it to measure the cross section below 14 MeV and bound it from below for energies above 14 MeV.
- [15] See Ref. [46] for discussion of energies below 15 MeV.
- [16] L. Alvarez-Ruso, M. Sajjad Athar, M. B. Barbaro, D. Cherdack, M. E. Christy, P. Coloma, T. W. Donnelly, S. Dytman, *et al.*, *Prog. Part. Nucl. Phys.* **100**, 1 (2018), arXiv:1706.03621 [hep-ph].
- [17] M. S. Athar and S. K. Singh, *Eur. Phys. J. Spec. Top.* (2021), 10.1140/epjs/s11734-021-00302-x, arXiv:2111.12328 [hep-ph].
- [18] M. B. Avanzini, M. Betancourt, D. Cherdack, M. D. Tutto, S. Dytman, A. P. Furmanski, S. Gardiner, Y. Hayato, L. Koch, K. Mahn, *et al.*, arXiv preprint (2021), arXiv:2112.09194 [hep-ex].
- [19] B. Abi *et al.* (DUNE Collaboration), *Eur. Phys. J. C* **80**, 978 (2020), arXiv:2006.16043 [hep-ex].
- [20] B. Abi *et al.* (DUNE), (2020), arXiv:2002.03005 [hep-ex].
- [21] Knowledge of energy resolution is more important for bias in extracted parameters than specific value of energy resolution. For the purpose of this study, which is focused on the effect of cross-section uncertainty, we assume that the detector response is perfectly known.
- [22] H. Minakata, H. Nunokawa, R. Tomas, and J. W. F. Valle, *JCAP* **12**, 006 (2008), arXiv:0802.1489 [hep-ph].
- [23] I. Tamborra, B. Müller, L. Hüdepohl, H.-T. Janka, and G. Raffelt, *Phys. Rev. D* **86**, 125031 (2012).
- [24] A. Gallo Rosso, F. Vissani, and M. C. Volpe, *J. Cosmol. Astropart. Phys.* **2017**, 036 (2017).
- [25] A. Gallo Rosso, F. Vissani, and M. C. Volpe, *J. Cosmol. Astropart. Phys.* **1804**, 040 (2018), arXiv:1712.05584 [hep-ph].
- [26] L. Wolfenstein, *Phys. Rev. D* **17**, 2369 (1978).
- [27] S. P. Mikheyev and A. Y. Smirnov, *Il Nuovo Cimento C* **9**, 17 (1986).
- [28] <http://phy.duke.edu/~schol/snowglobes/>.
- [29] <https://www.mpi-hd.mpg.de/personalhomes/globes/>.
- [30] S. Gardiner, *Phys. Rev. C* **103**, 044604 (2021), arXiv:2010.02393 [nucl-th].
- [31] S. Gardiner, *Comput. Phys. Commun.* **269**, 108123 (2021), arXiv:2101.11867 [nucl-th].
- [32] A. Mirizzi, I. Tamborra, H.-T. Janka, N. Saviano, K. Scholberg, R. Bollig, L. Hüdepohl, and S. Chakraborty, *Riv. Nuovo Cim.* **39**, 1 (2016), arXiv:1508.00785 [astro-ph.HE].
- [33] P. A. Zyla *et al.* (Particle Data Group), *Prog. Theor. Exp. Phys.* **2020**, 083C01 (2020).
- [34] This criterion is satisfactory given that the statistical regime is such that a Poisson distribution is well approximated by a Gaussian.
- [35] G. Cowan, K. Cranmer, E. Gross, and O. Vitells, *Eur. Phys. J. C* **71**, 1554 (2011), [Erratum: Eur.Phys.J.C 73, 2501 (2013)], arXiv:1007.1727 [physics.data-an].
- [36] R. Brun and F. Rademakers, *Nucl. Instrum. Meth. A* **389**, 81 (1997).
- [37] I. Gil-Botella and A. Rubbia, *J. Cosmol. Astropart. Phys.* **2003**, 009 (2003).
- [38] E. Kolbe, K. Langanke, G. Martínez-Pinedo, and P. Vogel, *J. Phys. G: Nucl. Part. Phys.* **29**, 2569 (2003).
- [39] N. Paar, H. Tutman, T. Marketin, and T. Fischer, *Phys. Rev. C* **87**, 025801 (2013), arXiv:1210.2655v1 [nucl-th].
- [40] T. Suzuki and M. Honma, *Phys. Rev. C* **87**, 014607 (2013), 1211.4078v1.
- [41] A. R. Samana, F. Krmpotić, and C. A. Bertulani, *Comput. Phys. Commun.* **181**, 1123 (2010).
- [42] M.-K. Cheoun, E. Ha, and T. Kajino, *Phys. Rev. C* **83**, 028801 (2011).
- [43] A. Samana and M. dos Santos, Private communication (2021).
- [44] A. R. Samana, C. A. Barbero, S. B. Duarte, A. J. Di-marco, and F. Krmpotić, *New J. Phys.* **10**, 033007 (2008).
- [45] C. A. Barbero, M. C. dos Santos, and A. R. Samana, *Braz. J. Phys.* **50**, 331 (2020).
- [46] F. Capozzi, S. W. Li, G. Zhu, and J. F. Beacom, *Phys. Rev. Lett.* **123**, 131803 (2019), arXiv:1808.08232 [hep-ph].
- [47] M. Bhattacharya, A. García, N. I. Kaloskamis, E. G. Adelberger, H. E. Swanson, R. Anne, M. Lewitowicz, M. G. Saint-Laurent, W. Trinder, C. Donzaud, *et al.*, *Phys. Rev. C* **58**, 3677 (1998).
- [48] W. Liu, M. Hellström, R. Collatz, J. Benlliure, L. Chulkov, D. C. Gil, F. Farget, H. Gräwe, Z. Hu, N. Iwasa, M. Pfützner, A. Piechaczek, R. Raabe, I. Reusen, E. Roeckl, G. Vancraeynest, and A. Wöhr, *Phys. Rev. C* **58**, 2677 (1998).

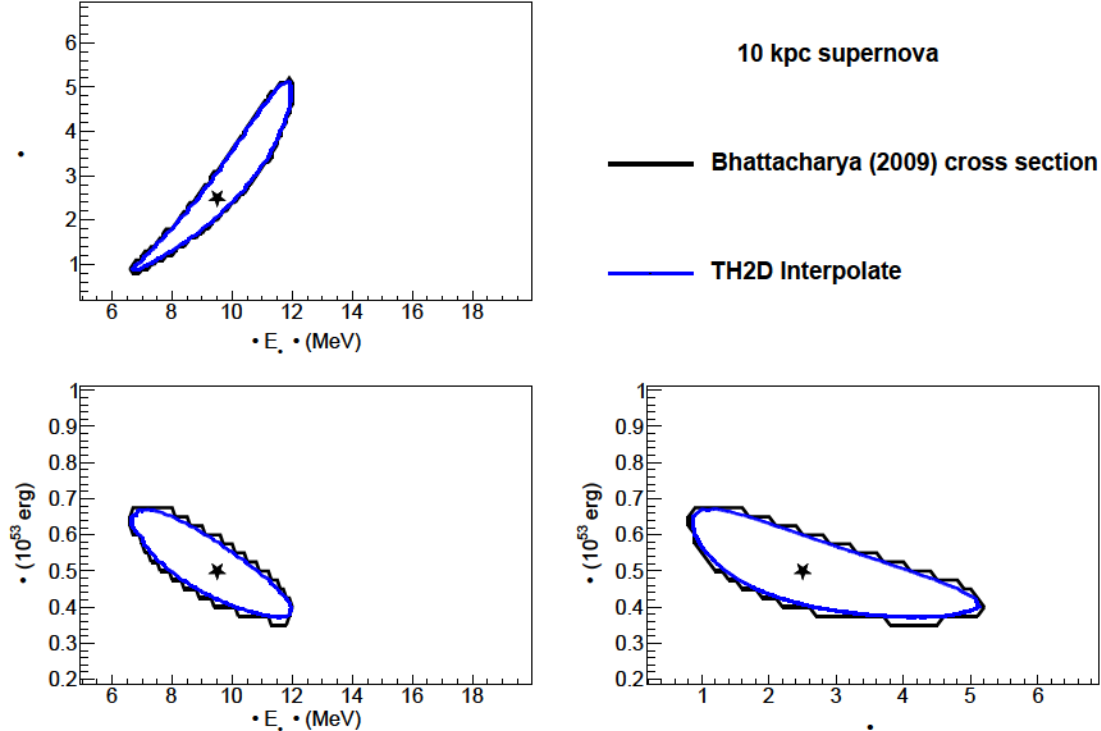


FIG. 21. 90% C.L. contours for the three parameter spaces with NMO assumptions and the MARLEY B 2009 cross section model [31]. The contours before interpolation have prominent jagged edges due to a limited number of reference grid points. The edges are most noticeable for the ϵ parameter.

- [49] M. Bhattacharya, C. D. Goodman, and A. García, *Phys. Rev. C* **80**, 055501 (2009).
- [50] For this paper, the reference cross section was calculated using the `ve40ArCC_Bhattacharya2009.react` configuration file.
- [51] A. R. Samana, F. Krmpotic, N. Paar, and C. A. Bertulani, *Phys. Rev. C* **83**, 024303 (2011), arXiv:1005.2134 [nucl-th].
- [52] D. N. Possidonio, R. C. Ferreira, A. J. Dimarco, C. A. Barbero, A. R. Samana, M. R. Azevedo, C. L. Santana, and A. E. Mariano, *Braz. J. Phys.* **48**, 485 (2018).
- [53] P. S. Barbeau, Y. Efremenko, and K. Scholberg, arXiv preprint (2021), arXiv:2111.07033 [hep-ex].
- [54] A. A. Aguilar-Arevalo *et al.* (CCM Collaboration), arXiv preprint (2021), arXiv:2105.14020 [hep-ex].
- [55] S. Ajimura, M. Botran, J. Choi, J. Choi, M. Cheoun, T. Dodo, H. Furuta, J. Goh, K. Haga, M. Harada, *Nucl. Instrum. Methods Phys. Res. A* **1014**, 165742 (2021), arXiv:2104.13169 [physics.ins-det].
- [56] D. Baxter, J. I. Collar, P. Coloma, C. E. Dahl, I. Esteban, P. Ferrario, J. J. Gomez-Cadenas, M. C. Gonzalez-Garcia, A. R. L. Kavner, C. M. Lewis, F. Monrabal, *et al.*, *J. High Energy Phys.* **2020**, 123 (2020).
- [57] K. J. Kelly, P. A. N. Machado, A. Marchionni, and Y. F. Perez-Gonzalez, *J. High Energy Phys.* **2021**, 87 (2021), arXiv:2103.00009 [hep-ph].
- [58] C. Grant and B. R. Littlejohn, arXiv preprint (2016), arXiv:1510.08431 [hep-ex].
- [59] W. Castiglioni, W. Foreman, B. R. Littlejohn, M. Malaker, I. Lepetic, and A. Mastbaum, *Phys. Rev. D* **102**, 092010 (2020), arXiv:2006.14675 [physics.ins-det].
- [60] N. Van Dessel, A. Nikolakopoulos, and N. Jachowicz, *Phys. Rev. C* **101**, 045502 (2020), arXiv:1912.10714 [nucl-th].
- [61] A. Bueno, I. Gil Botella, and A. Rubbia, (2003), arXiv:hep-ph/0307222 [hep-ph].
- [62] W. H. Press, B. P. Flannery, S. A. Teukolsky, and W. T. Vetterling, *Numerical Recipes in C: The Art of Scientific Computing* (Cambridge University Press, USA, 1988).